Finite element modelling of pipe piles driven in low-to-medium density chalk under axial loading

Kai Wen, PhD.; Research Fellow; **k.wen@soton.ac.uk; k.wen19@imperial.ac.uk**
Department of Civil, Maritime and Environmental Engineering, University of Southampton, Southampton SO16 7QF, UK; Formerly Department of Civil and Environmental Engineering, Imperial College London, SW7 2AZ London, UK

Stavroula Kontoe, Ph.D.; Associate Professor, skontoe@upatras.gr, Department of Civil Engineering, University of Patras, Patras 26504, Greece; Visiting Reader, stavroula.kontoe@imperial.ac.uk; Department of Civil and Environmental Engineering, Imperial College London, SW7 2AZ London, UK

Richard J. Jardine, Ph.D.; Professor of Geomechanics; r.jardine@imperial.ac.uk
Department of Civil and Environmental Engineering, Skempton Building, South Kensington Campus, Imperial College London, SW7 2AZ London, UK

Tingfa Liu, Ph.D.; Lecturer in Geotechnical Testing; tingfa.liu@bristol.ac.uk; tingfa-liu@hotmail.com
School of Civil, Aerospace and Design Engineering, University of Bristol, BS8 1TR Bristol, UK

Article type: General paper
Main text length (from Introduction to Conclusions, 7792 words)
Number of Figures: 19
Number of Tables: 5

ABSTRACT

Percussive driving in low-to-medium density chalk creates a thin annulus of fully de-structured 'putty' chalk around pile shafts and an outer annular zone where fracturing is more intense than in the natural chalk. This damage and the related generation, and subsequent equalisation, of excess pore pressures impacts the piles' time-dependent axial loading behaviour, as do other ageing processes. This paper presents finite element analyses of open steel tubular piles driven for the recent ALPACA and ALPACA Plus research projects under monotonic axial loading to failure after extended ageing periods. A nonlinear elastic stiffness model with a nonlocal deviatoric strain-based Mohr-Coulomb failure criterion was employed, with different sets of properties to represent the de-structured, fractured chalk and intact chalk. It is shown that the piles' axial responses are mainly controlled by the puttified chalk annuli. A simplified but efficient means is adopted to impose pre-loading chalk effective stress conditions that explicitly capture the effects of installation damage and subsequent ageing. The potential for strain-softening in the brittle chalk is examined and the effective stress paths developed in representative chalk elements throughout the loading are considered in conjunction with the mobilisation of accumulated deviatoric strains. The simulations indicate 264% higher shaft capacity in compression than in tension, which is mainly attributed to the internal chalk plug.

Keywords: finite element analysis; axially loaded driven piles; low-to-medium density chalk; offshore geotechnics

INTRODUCTION

Finite Element (FE) approaches have offered critical insights into the axial loading behaviour of open piles driven in many soil types, including clay tills and dense sands (see Jardine and Potts, 1988, 1993; Said et al., 2009; Han et al., 2018) and the 3-D behaviour of laterally loaded piles driven in similar strata (Byrne et al., 2020; Taborda et al., 2020; Zdravkovic et al., 2020; Hu et al., 2022). Such piles are used widely for supporting major offshore and onshore structures, including bridges, port facilities and offshore wind turbines. However, there has been little guidance regarding the axial loading behaviour and low bearing capacities shown by such piles driven in chalk, which is a very soft, brittle and sensitive, porous carbonate rock and widely distributed across Northwestern Europe and under the North and Baltic seas.

Working in conjunction with comprehensive field testing on piles driven in low-to-medium density chalk under the ALPACA and ALPACA Plus Joint Industry Projects (Jardine et al, 2023a, b), Wen et al. (2023a, 2023b) introduced a new 1-D 'Winkler' type monotonic axial load transfer model to compute the piles' axial load-displacement response. While this approach offers practical routes for designers, it provides limited insights into the detailed mechanics of pile-soil interactions that apply in-situ. Working in parallel with ALPACA, Pedone et al. (2023a) developed representative 3-D FE predictions for the piles' response to unidirectional, monotonic lateral loading in chalk through the ALPHA project (numerical Analysis of Laterally loaded Piles driven in cHAlk) project. This paper extends from the study by Pedone et al. (2023a) to address the remaining gap in knowledge regarding chalk-pile interactions under axial loading through fully non-linear axisymmetric FE simulations.

The comprehensive programmes of field ALPACA tests on highly-instrumented piles identified three phenomena that are critical to the monotonic axial loading response of piles driven in chalk:

i) Percussive pile driving creates a thin annulus of remoulded chalk putty around the pile shafts (Zone A) as well as an outer annular zone where the chalk develops markedly greater fracturing (Zone B). The properties within these zones are distinct from those applying in the parent natural chalk mass (Zone C).

ii) The local radial effective stresses developed along the pile shafts are very low at the end of driving but build greatly if the piles are allowed to age in-situ, leading to significant pile axial capacity growth, or set-up.

iii) The final distributions of shaft radial effective stresses depend critically on the local CPT resistance profiles and the relative heights h/R of each point above the pile tip, where R is the pile radius.

As in all FE simulations, it is critical to choose constitutive models that capture the media's mechanical behaviour adequately. The (undamaged) natural chalk mass encountered at the ALPACA St Nicholas-at-Wade (UK) test site shows brittle strain-softening behaviour under in-situ stresses (Vinck et al., 2022). Liu et al. (2023) shows that its behaviour is markedly pressure dependent, gradually transforming to being ductile and manifesting contraction response under p_0' levels higher than 1.0 MPa. It is well established that numerical simulations of strain-softening problems, in which strain localisation occurs within a zone of limited thickness, can lead to numerical instabilities and significant mesh dependency (Galavi & Schweiger, 2010; Summersgill et al, 2017a, 2017b). Conventional FE formulations, however, link the degree of softening to the current strain at a single calculation point only, resulting in individual

82 calculation points in the mesh experiencing high strains and excessive reduction in strength in
83 comparison to the surrounding points. To overcome this numerical problem, a range of non-local
84 defined models, which regulate the strain calculations to avoid excessive softening, have been proposed,
85 including the original formulation (Eringen 1981; Bazant et al. 1984), the overnonlocal method
86 (Vermeer and Brinkgreve, 1994) and the Galavi and Schweiger (2010) method. These approaches do
87 not alter the fundamental constitutive governing equations but consider the calculation of strain as a
88 non-local variable by spatially averaging the local variables within a weighted reference volume.
89 Pedone et al. (2023a) has employed the Galavi and Schweiger (or G&S) model in combination with a
90 nonlinear elastic strain-softening constitutive model for successfully reproducing the shearing
91 behaviour of SNW natural chalk mass.

92 Another issue that should be considered to achieve successful FE simulations of axial pile response in
93 chalk is the realistic simulation of the soil effective stress regime around the pile shaft in the pre-
94 monotonic loading stages. Although 'wished-in-place' pile installation treatments may be satisfactory
95 for lateral loading cases (as argued by Pedone et al. (2023a)), it can give highly inaccurate axial capacity
96 predictions for driven piles and are therefore unsuitable. Ideally, one should model the pile driving
97 process and the equalisation of excess pore pressure to obtain realistic soil stress regime prior to
98 monotonic loading as demonstrated by several researchers for other geomaterials (like sands)
99 employing both large-deformation FE simulations with adaptive meshing (Zhang et al. 2014; Yang et
100 al. 2020) and DEM approaches (Wang and Zhao 2014; Ciantia et al. 2019). Large displacement PFEM
101 techniques have also been applied in a numerical pile installation study for chalk by Previtali et al.
102 (2023). Analysts working with conventional FE treatments have to employ simplified procedures to
103 replicate the in-situ soil stress regimes after pile installation, subsequent pore-pressure equalisation and

ageing in-situ. For example, Said et al. (2010) successfully applied the widely used ICP-05 sand method (Jardine et al., 2005) in their FE pile simulations to quantify the limiting shaft shear stress and base resistance after pile installation in sands.

This paper reports extensive FE simulations of three steel pipe piles tested under monotonic axial loading in the ALPACA and ALPACA JIP Plus programmes. To account for the marked installation effects, the chalk domain adjacent to the pile shaft was divided mainly into three zones with different chalk properties. The fractured (Zone B) and intact chalk (Zone C) were modelled with an isotropic nonlinear strain-softening Mohr-Coulomb model combined with nonlocal regularisation, accounting for the chalks' brittle shear strength parameters. A conventional nonlinear elastic Mohr-Coulomb model was adopted for the puttified chalk (Zone A), with the parameters being calibrated against the advanced laboratory element tests. The developed numerical model was first validated against the field pile test outcomes, before employing it to interpret the shaft resistance distributions and stress paths invoked in the chalk mass, as well as other aspects that help identify the axial monotonic loading responses of pipe piles driven in low-to-medium density chalk.

FIELD PILE TESTS AND ALPACA-SNW APPROACH

The field tests considered below are a subset of those conducted for the ALPACA and ALPACA Plus JIPs. The piles were driven through the Margate and underlying Seaford chalk formations, which are structured, low-to-medium density, CIRIA Grade B2/B3 chalk, following Lord et al. (2002). An extensive set of cone penetration tests was carried out at the site, offering comprehensive profiles of cone resistances and sleeve friction (see Vinck et al., 2022). The water table lies at $\approx$5.5 to 6 m, with slight seasonal variations. Chalk above the water table is almost fully saturated and the natural (fractured)

chalk is assessed as having high mass hydraulic conductivities between 10^{-5} and 10^{-3} m/s. Further details on the ground profile are given by Buckley et al. (2018), Vinck et al. (2022) and Jardine et al. (2023a, 2023b).

Pile TP1, the largest driven pile for the ALPACA Plus JIPs, was selected as the main simulation case and supplemented by tests on two smaller LD06 and LD07 piles. As summarised in Table 1, Pile TP1 had an outer diameter (D) of 1.8 m and a wall thickness (t_w) of 25 mm. It was driven to the 18 m target tip depth by hydraulic hammers, with a stick-up of 3.5 m length left above ground level after installation. Pile TP1was then allowed to rest for 373 days prior to imposing tension loading with a computer-controlled hydraulic system with feedback from a load cell at the pile head. Sets of potentiometers were used to measure pile head displacements relative to a reference beam and two diametrically opposed strings of vertical Fibre Bragg Grating (FBG) optical sensors were mounted to measure axial strains at ten pile shaft levels. As seen in Table 1, pile LD06 had a smaller diameter and penetration depth, which was instrumented and tested in the same way after 211 days of ageing; pile LD07 was nominally identical to LD06 pile but was tested in compression after 260 days of ageing.

Table 1 Summary for driven piles simulated in this study

Driven pipe pile code	TP1	LD06	LD07
Axial load direction	Tension	Tension	Compression
Outer diameter, D [m]	1.8	0.508	0.508
Wall thickness, t_w [mm]	25	20.6	20.6
Pile embedment, L_p [m]	18	10.16	10.16
Stick-up length* [m]	3.5	1.5	1.5
Age [days]	373	211	260

***** Stick-up length represents the pile segment length left above ground level after installation

Jardine et al. (2023a) provide more details on the pile tests and their interpretation. They also set out the new ALPACA-SNW approach for estimating the long-term axial shaft resistances at failure (τ_{rzf}), as given by Equation (1), which captures the very strong variations of local shaft capacity in chalk with CPT tip resistance (q_t), ratio of the vertical distance from the pile tip to pile radius (h/R), and loading sense in additional to water table position and pile tip conditions (open versus closed).

$$\tau_{rzf} = f_L \left[\sigma_{rc}^{'} + \Delta\sigma_{rd}^{'} \right] \tan \delta^{'} \quad (1)$$

where f_L is loading factor; values of 2/3 and 4/3 are recommended for tension and compression piles respectively. $\sigma_{rc}^{'}$ is the local radial effective stress along the pile shaft after equalisation and prior to loading, which depends on the relative water table depth, q_t and h/R, as expressed by Equations (2) and (3) set out below; $\Delta\sigma_{rd}^{'}$ denotes change in radial effective stress due to interface dilation; $\delta^{'}$ is chalk-steel interface friction angle that can be determined from representative ring-shear interface tests.

Above water table: ($h/R \geq 4.0$)

$$\sigma_{rc}^{'} = f_{tip} \times 0.078 \times q_t \times (h/R)^{-0.85} \quad (2)$$

Below water table: ($h/R \geq 0.5$)

$$\sigma_{rc}^{'} = f_{tip} \times 0.025 \times q_t \times (h/R)^{-0.80} \quad (3)$$

where f_{tip} is a pile tip condition factor, taken as 1 for open-ended piles with $15.4 \leq D/t_w \leq 70.8$ and 3 for closed-ended piles. The applicability of the above equations has been checked recently by against an independent set of high-quality field pile tests conducted at other chalk sites, collated by Vinck

(2021). The initial profiles of $\sigma_{rc}^{'}$ that were used as input for the simulations of piles TP1, LD06 and LD07 were based on these expressions above.

FINITE ELEMENT MODEL AND CALCULATION PHASES

The finite element analyses were carried out within the PLAXIS 2D V22.01, employing user-defined constitutive models and taking advantage of the axisymmetric nature of the problem by treating the pile centre as the axis of symmetry. Figure 1 shows the layout of the TP1 numerical pile model, with $x = 0$ being the pile's central axis. Horizontal and vertical fixities were applied at the bottom boundary, which was set at 30 m below ground level (bgl) to avoid any boundary effects. The vertical boundary in the radial direction, at which orthogonal movements were prevented, was located 25 m from the pile axis. Groundwater table was set at 6 m bgl, consistent with the field measurements.

The chalk domain above the pile tip level and outside of the pile shaft was divided into three vertical zones. The annular thickness of the first, puttified zone (Zone A) was assumed (from ground surface to the pile tip) equal to t_w, while the additionally fractured zone (Zone B) was taken as $5t_w$ thick. Note that the latter limits were adopted by Pedone et al. (2023) on the basis of chalk damage observations made by Buckley et al. (2018) around open steel piles driven at SNW. The same limits are also broadly compatible with the later observations made around the larger diameter ALPACA Plus piles (Jardine et al. 2023a). Although no supporting information was available in the literature, a 0.5 m deep 'fractured chalk' zone was assumed to apply below the pile tip. The piles' internal core was treated as having the shearing properties of the de-structured (puttified) chalk, as supported by the numerical simulation of pile installation in chalk by Previtali et al. (2023), while its stiffness properties differed slightly from those applied in Zone A (see Wen (2023)).

Figure 1 also shows the discretization of the chalk domain into 5129, 15-noded, triangular elements with 12 gauss points each. Note that finer discretization was adopted close to the pile, where stress concentrations are anticipated. The internal and external chalk-pile interfaces were modelled using "zero-thickness" interface elements. The steel piles were treated as linear elastic materials and were discretised into 1863 elements of the same type to that employed for the chalk domain, with a steel unit weight of 78.5 kN/m^3, a Young's modulus of 210 GPa and a Poisson's ratio of 0.28.

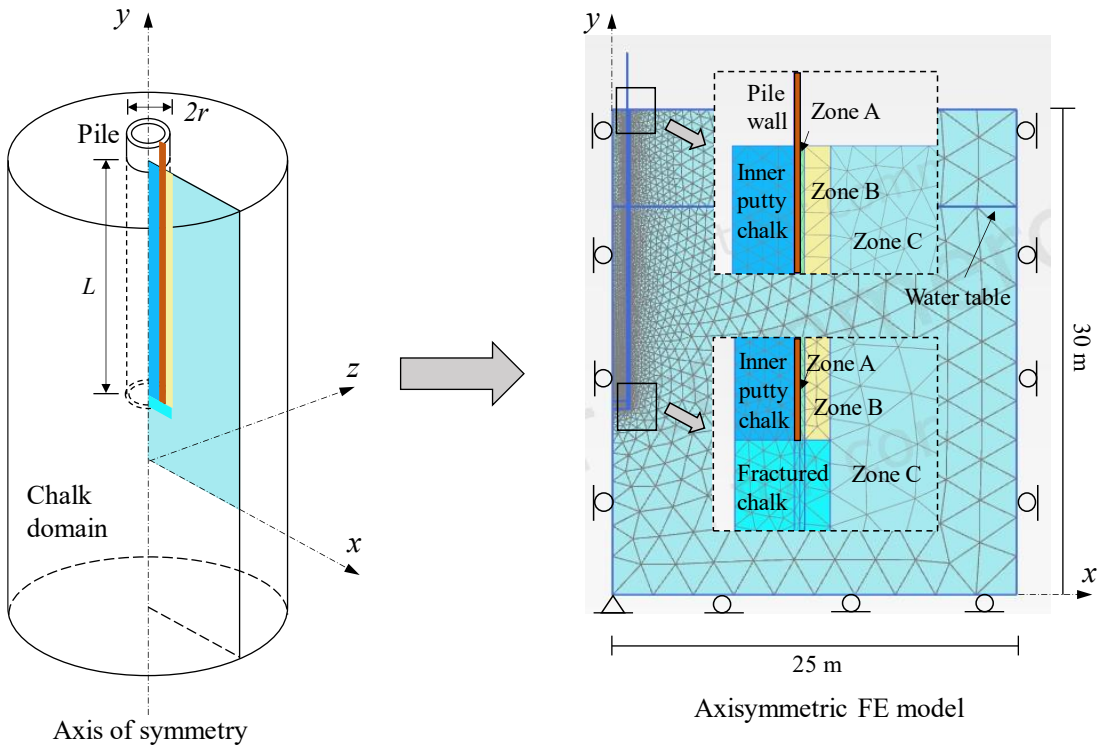


Figure 1 Axisymmetric FE model of TP1 pile under axial loads and the finite element mesh

Description of calculation phases

Figure 2 shows the four calculation phases specified for the modelling of the monotonic axial loading response, covering (i) the initialisation of geostatic conditions within the entire chalk domain, (ii) the application of the ALPACA-SNW radial effective stress, (iii) the activation of the pile wall and (iv) the

application of monotonic compression/tension at pile head. Given the relatively high in-situ permeability of the chalk mass, all the calculation phases were performed assuming drained conditions.

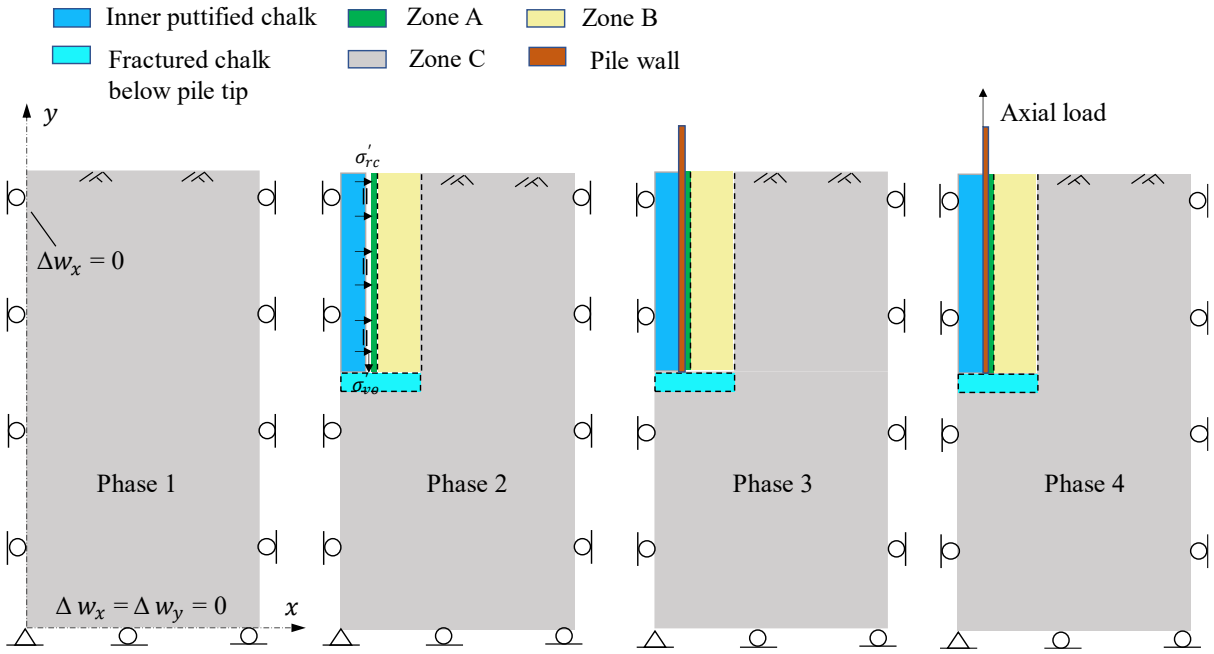


Figure 2 The four calculation phases adopted for simulating driven piles in chalk

In the first phase, the chalk domain was treated as a uniform undamaged intact material, reproducing the geostatic stress state before pile installation. A coefficient of earth pressure K_0 of 0.6 was adopted following Pedone et al. (2023a). It is acknowledged however that other K_0 values have been estimated for chalk in earlier studies. For instance, Schwamb and Soga (2015) assumed a K_0 of 1.0 in their simulation of a wished-in-place diaphragm wall, while Nejjar et al. (2019) adopted 0.43 for the chalk strata encountered in the Grand Paris project.

The second phase was designed to achieve a realistic radial effective stress field (σ'_{rc}) after pile installation and pore pressure equalisation. Clusters representing the puttified chalk (inside and outside the pile wall) and fractured chalk (including the zone beneath the pile base) were activated, whereas the cluster representing the pile wall in the next phase was excavated, resulting in a void in the FE model.

Consequently, the distribution of σ'_{rc} calculated from Equations (2- 3) was imposed as an external stress boundary condition in the void along the Zone A, approximated by a multilinear variation of stresses with depth, effectively representing a cylindrical cavity expanding out into the chalk mass. In the meantime, the estimated in-situ geostatic vertical effective stress σ'_{v0} was applied along the cavity base. Apart from that, horizontal fixity was set up along the cavity left boundary to prevent it from collapsing, leaving the inner puttified chalk column under geostatic conditions.

Once the second calculation phase was completed, the imposed σ'_{rc} distribution, base pressure and the relevant constraints along the inside puttified chalk were removed. Meanwhile, any chalk displacements induced in the previous phase were re-zeroed before the pile cluster was activated. This allowed the radial stress field adjacent to the pile to be close to the ALPACA field trends (as discussed later) and ensured zero pile head displacement before imposing any external axial load. Note that this simulation neglected any potential residual stresses locked in the piles during installation.

Finally, monotonic (and rate independent) pile loading was simulated by imposing upward (tension) or downward (compression) pile head displacements, covering the full range up to peak load, or displacements exceeding D/10.

CONSTITUTIVE MODELS AND INTERFACE MODEL

Isotropic non-linear stiffness model with non-local strain-softening Mohr-Coulomb failure criterion

A user-defined constitutive model was employed to simulate the chalk which combined a small-strain stiffness model with a strain-hardening/softening Mohr-Coulomb failure criterion based on the non-local total deviatoric strain (Taborda et al. 2016; Taborda et al. 2022a, 2022b). The non-local deviatoric

strain was defined based on the Vermeer and Brinkgreve (1994) ovenonlocal method through two user-specified parameters, the defined length (DL) and α. The former parameter impacts on the weighting function that prevents the formation of a concentrated strain peak, providing a more uniform distribution of strains across the slip surface, while the latter parameter controls the contribution of the local strain at the calculation point to the final non-local strain value (Summersgill et al. 2017b).

Regarding the elastic behaviour in the employed constitutive model, the shear modulus of the material is calculated using:

$$G_{tan} = G_{max} \cdot R_G \tag{4}$$

$$G_{max} = G_0 \cdot f_G(e) \cdot \left(\frac{p'}{p'_{at}}\right)^{m_G} \tag{5}$$

where G_{max} is the current maximum shear modulus, G_0 is the small-strain stiffness, $f_G(e)$ specifies how, under given stress and strain conditions, G_{max} varies with void ratio (in the present study $f_G(e)$=1), p' is the mean effective stress, p'_{at} is atmosphere pressure (= 101.3 kPa) and m_G is a material constant (Taborda et al. 2022a, 2022b).

The variable R_G in Equation (4) denotes a reduction factor associated with the deviatoric deformation level (E_d^*), as expressed by:

$$R_G = R_{G,min} + \frac{1 - R_{G,min}}{1 + \left(\frac{E_d^*}{n \cdot a_0}\right)^b} \tag{6}$$

where $R_{G,min}$ is the normalized degradation limit for G_{tan}, n is a scaling factor, a_0 is a basic degradation parameter for G_{tan} and b controls the degradation nonlinearity of G_{tan} (Taborda et al. 2022a, 2022b).

The yield surface is defined by a strain-hardening/softening Mohr-Coulomb failure criterion:

$$F = J - \left(p + \frac{c'}{\tan\varphi'}\right) \cdot g_i(\theta) = 0 \tag{7}$$

where c', φ' and $g_i(\theta)$ are associated with the current soil strength, which are evaluated based on the current non-local deviatoric strain E_d^{nl} (defined as a weighted average of the deviatoric strain taking place within a weighted reference volume). The detailed formulations of the gradient of yield surface and hardening modulus can be found in Taborda et al. (2022a, 2022b).

Figure 3 shows how the strength parameters vary with E_d^{nl} in three divided zones. In Zone 1, c' and φ' are assumed to increase linearly from initial values (c_i' and φ_i') to peak values (c_p' and φ_p') corresponding to $E_{d,1}^{nl}$; in Zone 2, c' and φ' remain constant and equal to the peak values; in Zone 3, c' and φ' start to reduce from the peak values at $E_{d,2}^{nl}$ to residual values (c_f' and φ_f') corresponding to $E_{d,3}^{nl}$, as given by the Equations (8), (9).

$$\varphi' = \varphi_f' + \frac{\varphi_p' - \varphi_f'}{E_{d,2}^{nl} - E_{d,3}^{nl}}\left(E_d^{nl} - E_{d,3}^{nl}\right) \tag{8}$$

$$c' = c_f' + \frac{c_p' - c_f'}{E_{d,2}^{nl} - E_{d,3}^{nl}}\left(E_d^{nl} - E_{d,3}^{nl}\right) \tag{9}$$

Having briefly introduced the characteristics of the employed constitutive model, the subsequent sections describe the calibration of chalk's relevant properties in various zones separately, covering (1)

pre-yield shearing behaviour (stiffness evolution); (2) shearing strength properties within the modified Mohr-Coulomb framework; (3) parameters defining the non-local regularisation and the associated strain-softening rate.

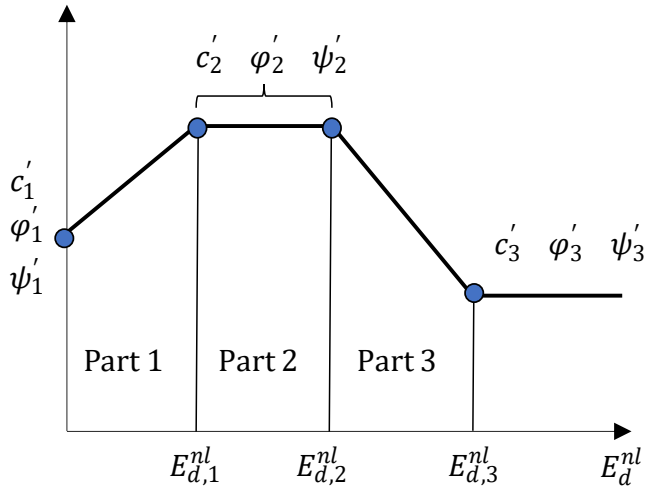


Figure 3 Variation of strength parameters c', $\varphi'$and ψ' with the current nonlocal strain (Taborda et al. 2022a, 2022b)

Calibration of nonlinear stiffness properties

Table 2 summarises the relevant nonlinear small strain stiffness parameters for all chalk domains involved. Note that these parameters are calibrated against high-quality in-situ and laboratory element tests by Vinck et al. (2022) and are generally consistent with the values adopted by Pedone et al. (2023a) for FE analysis of laterally loaded driven piles in chalk.

Based on the triaxial test measurements by Vinck et al. (2022) on the natural chalk specimens under various in-situ p_0' values, Pedone et al. (2023a) carried out a detailed 3D FE simulation of the Vinck et al. (2022) triaxial tests to capture the pre-yield nonlinear stiffness of intact chalk, treating the initial shear modulus G_0 as being isotropic and independent of the mean effective stress p'. Their simulations approximated the initial maximum $G_0 = 2$ GPa in conjunction with a Poisson's ratio of $\nu = 0.2$, which

results in a reasonable reproduction of the laboratory samples' pre-yield stiffness degradation. However, this set of parameters is not representative of the chalk mass' field response due to the presence of meso- and macro- scale vertical fissures which are largely avoided when preparing laboratory test specimens. To account for the in-situ fissuring and following the elastic axial loading analyses of the pile tests reported by Jardine et al (2023a, 2023b), Pedone et al. (2023a) argued that the maximum field shear moduli of the intact chalk mass (Zone C) are approximately 25% of the equivalent isotropic shear modulus calculated from the locally instrumented triaxial tests, leading to a $G_0 = 0.5$ GPa.

The maximum shear modulus of Zone B chalk was taken as being an order of magnitude lower, giving $G_0 = 0.05$ GPa, as suggested by Clayton et al. (2002) and Pedone et al. (2023a). Again, the same non-linear stiffness degradation curve was applied as the one adopted for Zone C from laboratory element tests.

Table 2 Calibration of pre-yield stiffness and strength parameters applied in different chalk domains

Parameters	Zone A	Zone B	Zone C	Inner puttified chalk	Fractured chalk below the pile tip
Stiffness-related parameters					
G_0 [MPa]	1000	50	500	1000	300
Poisson's ratio ν	0.2	0.2	0.2	0.2	0.2
$f_G(e)$	1	1	1	1	1
m_G	0	0	0	0	0
a_0	3.5E-5	1E-3	1E-3	3.5E-5	1E-3
b	1.3	4	4	1.3	4
$R_{G,min}$	0.01	0.2	0.2	0.01	0.2
G_{min} [MPa]	10	10	100	100	100
Strength-related parameters (nonlocal strain softening analysis)					
Strain-Softening	×	√	√	×	√
c'_p [kPa]	3	159	747	3	159
c'_f [kPa]	3	5	5	3	5

φ_p' [°]	31.5	29	29	31.5	29
φ_f' [°]	31.5	31.5	31.5	31.5	31.5
ψ [°]	0	0	0	0	0

Considering the thin annular puttified chalk zone adjacent to the pile shaft, Doughty et al. (2018) noted that the G_0 values developed by the puttified chalk grow with age, while their degradation curves become steeper. This study adopted an initial maximum shear modulus of $G_0 = 1.0$ GPa for the Zone A chalk, which was assumed to be constant with depth, while the potential G_0 dependency on p' was neglected, as in Pedone et al. (2023a). Figure 4 shows the degradation of shear modulus with deviatoric strain invariant adopted in FE analyses (defined in Equations (4, 5, 6), which well reflects the experimental trend obtained from a triaxial test on 30-days aged puttified chalk (Vinck 2021). Wen (2023) noted the uncertainties in calibrating stiffness parameters for the inner puttified chalk plug and the fractured chalk zone below the pile tip and undertook extensive sensitivity studies that led to the final model parameters listed in Table 2.

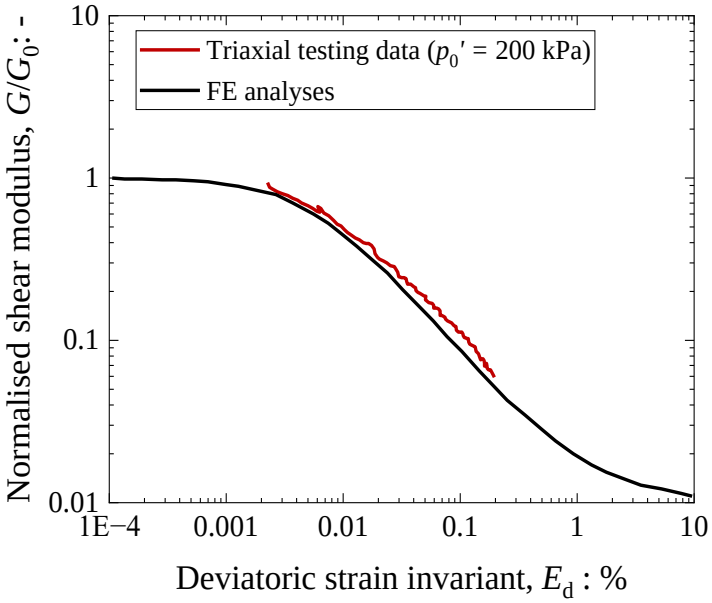


Figure 4 Stiffness degradation data (from Vinck 2021) and stiffness degradation curve adopted in FE analyses for 30-days aged puttified chalk (adapted from Pedone et al. 2023a)

Calibration of shear strength parameters

Table 2 also summarises the shear strength parameters adopted for the chalk zones in the nonlocal strain softening analysis, while Table 3 lists those employed in the nonlinear elastic perfectly plastic analyses, as discussed later. Vinck et al. (2022) reported the peak, ultimate and post-rupture shearing resistances (as defined by Burland (1990)) mobilised in intact chalk specimens under drained triaxial testing conditions. As shown in Figure 5, while the gradient of the peak, post-rupture and ultimate strength envelopes show slight variations with p', Pedone et al. (2023a) treated them as linear functions of p' within the range of 34 kPa ~ 3200 kPa. The Mohr-Coulomb peak shear strength parameters for the Zone C chalk over this range were approximated as $c'_p = 747$ kPa and $\varphi'_p = 23.9°$, while the ultimate shear strength parameters were $c'_f = 0$ kPa and $\varphi'_f = 31.5°$.

Table 3 Strength-related parameters applied in various zones in the nonlinear elastic perfectly plastic analysis

Parameters	Zone A	Zone B	Zone C	Inner puttified chalk	Fractured chalk below the pile tip
c'_p [kPa]	3	159	159	3	159
c'_f [kPa]	3	159	159	3	159
φ'_p [°]	31.5	29	29	31.5	29
φ'_f [°]	31.5	29	29	31.5	29
ψ [°]	0	0	0	0	0

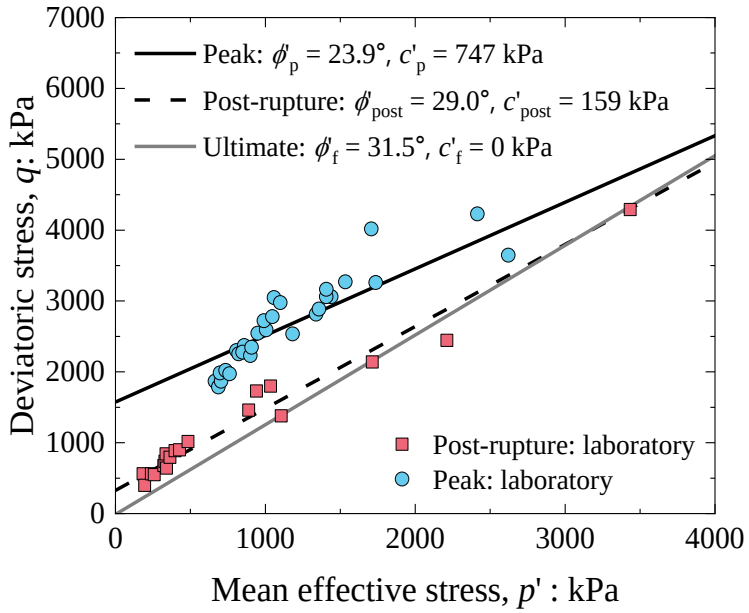


Figure 5 Drained triaxial test on intact chalk from Vinck et al. (2022) and the derived failure envelopes (adapted from Pedone et al. 2023a)

It is recognised that the strength parameters of Zone B chalk are challenging to calibrate directly based on laboratory element tests, as they represent an unsampled volume of material with more intense than natural fracturing damage caused by pile installation. The Pedone et al. (2023a) approach was adopted in which the peak strength parameters of Zone B chalk were set equal to the post-rupture strength of Zone C, giving $c'_p = 159$ kPa and $\varphi'_p = 29°$ for Zone B chalk (see Figure 5), which then reduced to the same ultimate shaft strength as Zone C.

The puttified chalk in Zone A was simulated with a perfectly plastic Mohr-Coulomb model, with the strength parameters corresponding to a nominal $c' = 3$ kPa and $\varphi' = 31.5°$ (see Figure 5), close to the ultimate strength of Zone C chalk under high confining pressure.

For simplicity, the shear strength parameters for the last two zones, namely the inner puttified chalk zone and the fractured chalk below pile tip, are the same as the ones in Zone A and Zone B respectively. A global dilatancy angle of $\psi = 0°$ was considered for all chalk zones, following Pedone et al. (2023a).

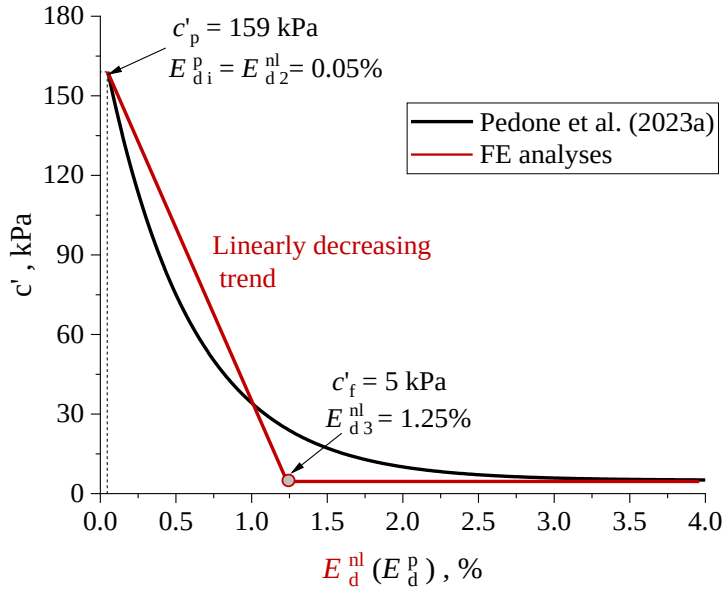
This was taken as the most representative choice given the broad mix of both dilative and contractive behaviour invoked by pile axial loading.

Nonlocal strain-softening parameters

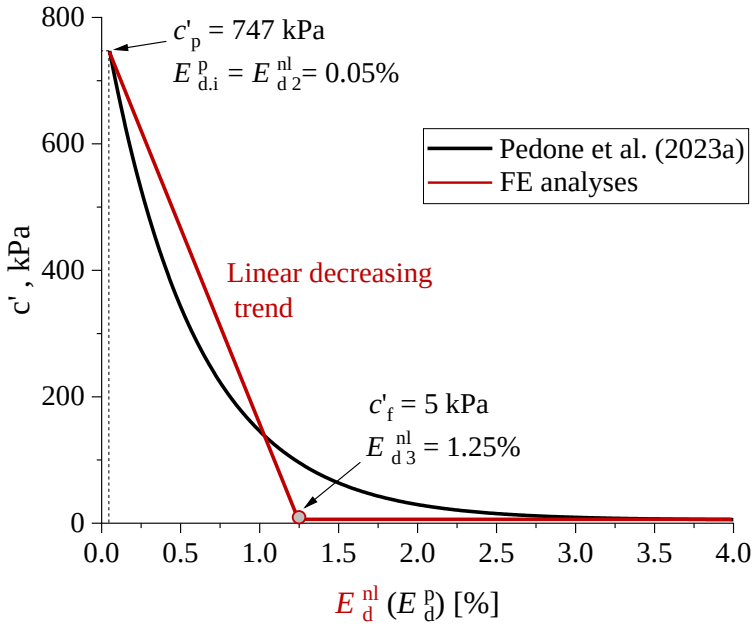
The first aspect to consider is the definition of the non-local deviatoric strain E_d^{nl}, by choosing appropriate α and DL values. A DL value of 0.25 m was adopted in this study, which is consistent with Pedone et al. (2023a), while α = 1.5 was used as recommended by Summersgill et al. (2017a). Another aspect to consider is the parameters that control the strength reduction rate relating to the accumulated E_d^{nl} for the fractured chalk and intact chalk (i.e. $E_{d,2}^{nl}$, $E_{d,3}^{nl}$). Figure 6 compares the calculated exponential decay of c' along with the parameters suggested in Pedone et al. (2023a) with the linearly decreasing trends in this study (using Equations 8, 9). The present study adopted a representative set of parameters $E_{d,2}^{nl} = 0.05\%$ and $E_{d,3}^{nl} = 1.25\%$ for both the fractured and intact chalk, as summarised in Table 4.

Table 4 Parameters related to the non-local formulation and the strain-softening rate for different chalk zones

Parameters	Zone A	Zone B	Zone C	Inner puttified chalk	Fractured chalk below the pile tip
Strain-Softening	×	√	√	×	√
DL [m]	0.25	0.25	0.25	0.25	0.25
α	1.5	1.5	1.5	1.5	0.15
$E_{d,2}^{nl}$ [%]	-	0.5	0.5	-	0.5
$E_{d,3}^{nl}$ [%]	-	1.25	1.25	-	1.25



(a)



(b)

Figure 6 Calibration of $E_{d,2}^{nl}$ and $E_{d,3}^{nl}$ parameters for: (a) fractured chalk; (b) intact chalk

Interface model and parameter determination

The mechanical characteristics applying at the pile-chalk interface were assumed to follow a Coulomb failure criterion, of which the main strength properties include the friction angle (φ_i'), cohesion (c_i'), dilatancy angle (ψ_i'). Ziogos et al. (2017) obtained ultimate interface shear friction angles in the range

of 22°-40° based on interface shear tests on chalk. Vinck et al. (2023a) conducted a series of steel-chalk interface shear tests after extended ageing periods with different combinations of steel types and chalk pore water chemistry. Vinck et al. (2023a) shows that, for aged puttified chalk under free air access conditions, the ultimate frictional angle of the chalk-oxidizable steel interface varies significantly, with a range of 34.5˚±1.28˚, which exceeds the puttified chalk's angle of shearing resistance at critical state of around 31º~32º. In any unconstrained system, this would force the failure into the putty chalk.

In the present study, a small cohesion c_i' (around 3 kPa to ensure numerical stability) and a slightly lower interface φ_i' (= 30.5˚) were chosen based on the extensive parametric study carried out by Wen et al. (2023a) and Wen (2023). Note that the interface dilation angle ψ_i' was set to 0, consistently with the adjacent puttified chalk. With respect to the elastic interface normal/shear stiffness K_n/K_s (in kN/m^3), as there is no widely adopted guidance or experimental evidence, their values (K_s= 3.0E5 kN/m^3; K_n = 2.5E6 kN/m^3) were determined after a performing a sensitivity study (see Wen (2023)), similar to the approach taken in the simulation of laterally loaded piles in chalk by Pedone et al. (2023a, 2023b). Note that these interface parameters applied to all the piles simulated in the present study.

RESULTS AND DISCUSSION

This section examines first the effectiveness of generating the stress regime in the vicinity of the pile employing the long-term ALPACA-SNW empirical expression. This simplified approach accounts indirectly for pile driving effects as well as for time related stress changes due to ageing. Its effectiveness is assessed based on the simulation of a monotonic tension test on TP1, examining mobilised shaft resistances, the stress paths of representative elements in the three chalk zones and the underlying chalk-pile interaction mechanism.

The adjustment of soil stress field around pile shaft

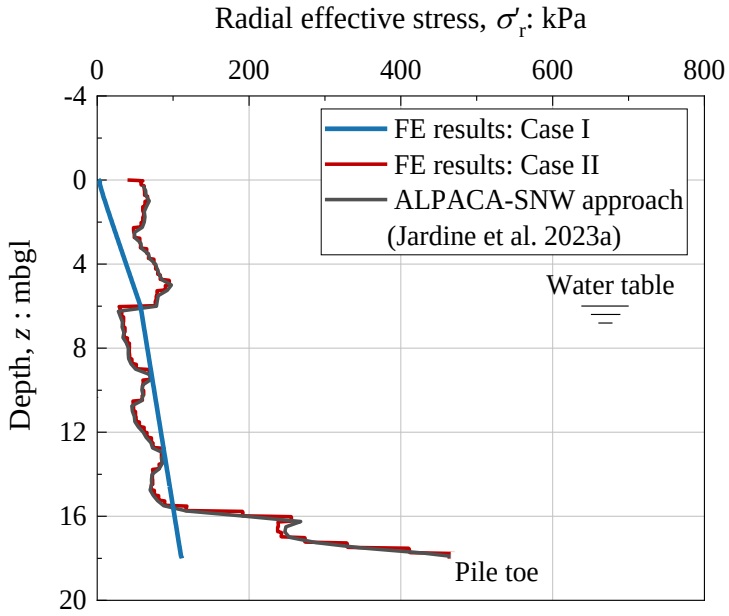
Two cases were considered in this study to demonstrate how the adopted modelling strategy can adjust the soil stress regime in the pile vicinity. In Case I, geostatic ground conditions were assumed, and the pile was wished-in-place. In Case II, which is considered as the reference case for all remaining analyses, the radial shaft stress profile was specified based on the long-term ALPACA-SNW approach, applying as a stress boundary along the side of Zone A (see Figure 2).

Figure 7(a) shows the computed distributions of σ_r' on the pile shaft in the pre-monotonic loading phases for the two cases, along with the ALPACA-SNW predictions. In Case I, σ_r' exhibits a linear increase with depth over a zone up to 6.0 m bgl., followed by a more moderate increase with depth below the water table. As expected, the σ_r' profile from Case I generally falls below the ALPACA-SNW prediction, except over the depth range of 6.0 m – 12.0 m bgl where Case I manifests slightly higher values. In Case II, as expected, the derived σ_r' profile from numerical model is nearly identical to the ALPACA-SNW prediction, indicating the validity of the adopted simplified simulation strategy.

Figure 7(b) compares the variation of $\sigma_r'/\sigma_{r=R}'$ with the r/R obtained for the two cases. Two representative elevation levels corresponding to a lower and higher h/R (h/R = 2.2, 15.6) are selected for illustration purposes, where h is the distance from the pile tip. In Case I, constant $\sigma_r'/\sigma_{r=R}'$ of 1.0 is observed over the radial distance away from the pile shaft as expected. In Case II, both curves show semi-logarithmical decay with r/R from the pile axis towards K_0 values at around $r/R = 5{\sim}10$. This is broadly consistent with the experimental observations made by Bond and Jardine (1991) in stiff clays at lower h/R elevations, but it does not reflect the typical trends shown at higher h/R elevations round closed-ended piles installed in dense sand, where σ_r' has a peak at $r/R = 3{\sim}4$, followed by a reduction toward $K_0\sigma_v'$ value at greater r/R (see Jardine et al. 2013; Yang et al. 2020). It should be recognised

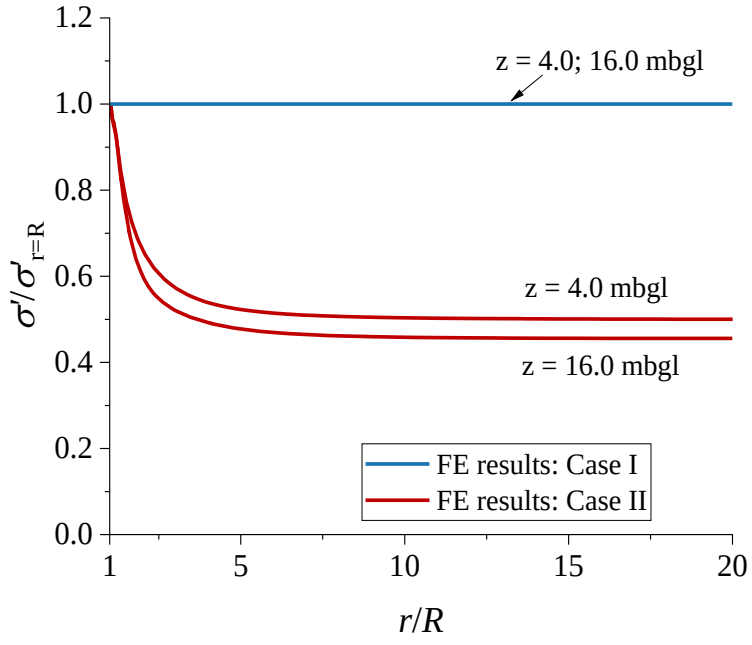
389 that this simplified approach cannot simultaneously reproduce the circumferential, radial and vertical

390 effective stress state around driven piles.



391

392 (a)



393

394 (b)

395 Figure 7 Comparison between two cases for pile TP1: (a) radial effective stress profile; (b) variation
396 of radial effective stress against normalised radius obtained from FE simulations

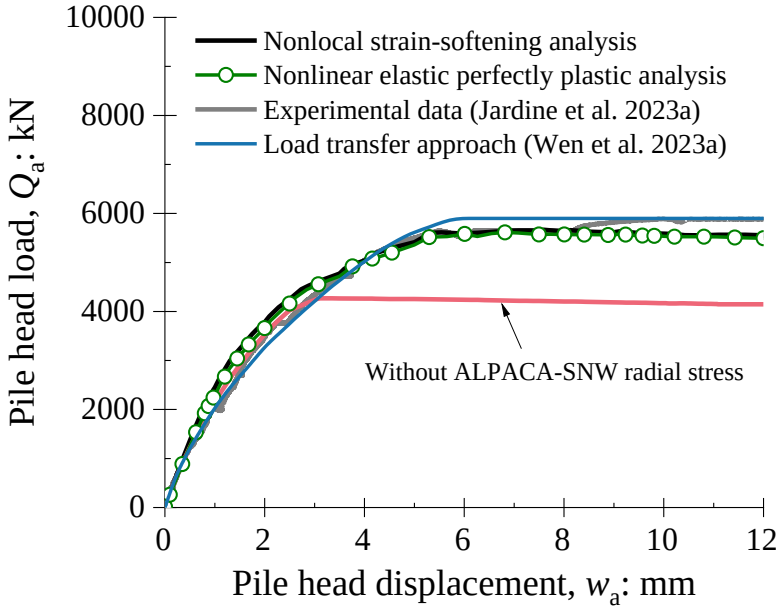
FE model verification against field measurements

Figure 8(a) compares the experimental and numerically predicted load-displacement curves for the tension pile TP1. Apart from the reasonable match with the measured ultimate capacity, the numerical model provides reasonable prediction of axial stiffnesses throughout the loading. Also plotted in Figure 8(a) is the load-displacement prediction made without applying the ALPACA-SNW radial effective stress profile. Note that in this case, the puttified chalk was also treated as a non-linear elastic, perfectly plastic, Mohr-Coulomb material, whereas the remaining chalk material was assumed to follow the nonlocal defined strain-softening Mohr-Coulomb failure criterion. The numerical model without applying the ALPACA-SNW stresses predicts an ultimate capacity approximately 30% lower than the field measurement, whereas the initial stiffness of load displacement response appears to be reasonably well predicted with and without the application of the ALPACA-SNW stresses. As pile displacements over the earlier stages of loading are primarily controlled by the pile compressibility and stress-independent elastic modulus assumed in the chalk domain (Wen et al. 2023a), both analyses capture the early part of the load displacement response similarly well.

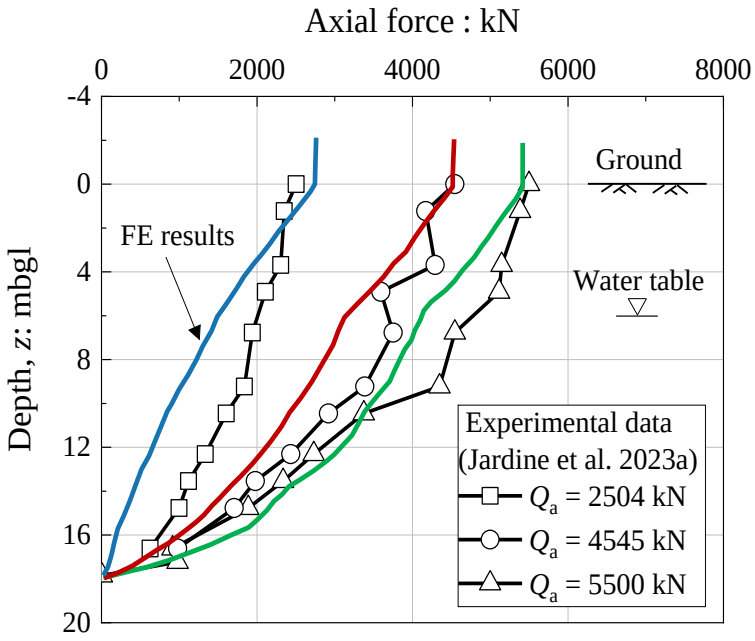
Figure 8(a) also illustrates the predicted load-displacement curve using the nonlinear elastic perfectly plastic constitutive models for all chalk domains, with the stiffness and strength parameters given in Table 2 and Table 3 respectively. Note that in the 'nonlinear elastic perfectly plastic analysis' the strain nonlocalisation formulation was not deployed. As seen in Figure 8 (a), the predictions of axial capacity and stiffness evolution trends are nearly identical to those from the 'nonlocal strain-softening' analyses, implying that any strain-softening features within the chalk Zones B and C play a marginal role in such analyses. This statement is further supported by the limited evolution of the current hardening parameters (c' and φ') in these two zones throughout loading, as presented subsequently. Also plotted

in Figure 8(a) is the predicted load-displacement response by the 'chalk-specific' Winkler soil spring model ('t-z' model in this case) proposed by Wen et al. (2023a, 2023b), which also generates a good match to the experiment data.

Figure 8(b) compares the calculated and measured (via the FBG strain gauges) axial force profiles for the TP1 pile for the reference Case II. In general, the axial force profiles show a similar pattern at different phases of axial pile head loading. Broad agreement with the experimental data is observed as the pile approaches failure (Q_a = 5500 kN), indicating that the adopted computational approach makes reasonable prediction of the axial force transfer at the ultimate state. At lower axial loads, although the match is reasonable at shallow depths, the FE model consistently underestimates the axial pile forces below 4.0 m bgl. Differentiation with respect to depth of the axial force distribution leads to predictions for the mobilisation of local shaft resistances which confirm the deviations seen in some profiles at depths below 2.0 m. Note that deflection points on the axial force profiles are expected near the water table depth, due to the separate (and discontinuous) consideration of shaft resistances below and above water table according to the long-term ALPACA-SNW approach.



(a)



(b)

Figure 8 (a) Comparison between experimental and numerical load-displacement curves; (b) comparison of axial force profiles

Predicted loading response of pile TP1

The FE analyses of pile TP1 for the reference Case II resulted in the profiles of local shaft displacement shown in Figure 9, corresponding to pile head displacements w_a = 2.0, 4.0 and 8.0 mm. As discussed in Wen et al. (2023b), the total pile head displacements can be separated into parts: an overall 'rigid' motion plus elastic pile stretch (in tension) or shortening (in compression). The former component can be roughly inferred from the pile tip movement, whereas the latter is considered as the difference between pile head and tip displacements. At $w_a = 2.0$ mm, the TP1 pile's elastic stretch is around 1.5 mm, accounting for roughly 75% of the pile head displacement. However, at w_a = 4.0 mm, the pile rigid motion is seen to play a more important role as compared to the pile elastic stretch (around 55% of current total w_a). The pile stretch remains approximately constant once the pile shaft resistances are

fully mobilised. Also plotted in Figure 9 are the predicted local shaft displacement profiles from the load transfer model developed by Wen et al. (2023a, b), showing a pattern that is broadly consistent with the FE results.

Figure 10 plots the computed profiles of external pile shaft resistance throughout the axial loading. As the pile is loaded progressively towards failure, the local external shaft resistances are first fully mobilised at shallow depths and remain unchanged as w_a increases further. The local shaft resistances seem to be mobilised fully at w_a = 8.0 mm, leading to an axial ultimate capacity of 5500 MN. As noted earlier, shaft friction reductions were predicted near the water table level, due to the different shaft resistance expressions applied below and above water table in the ALPACA-SNW approach.

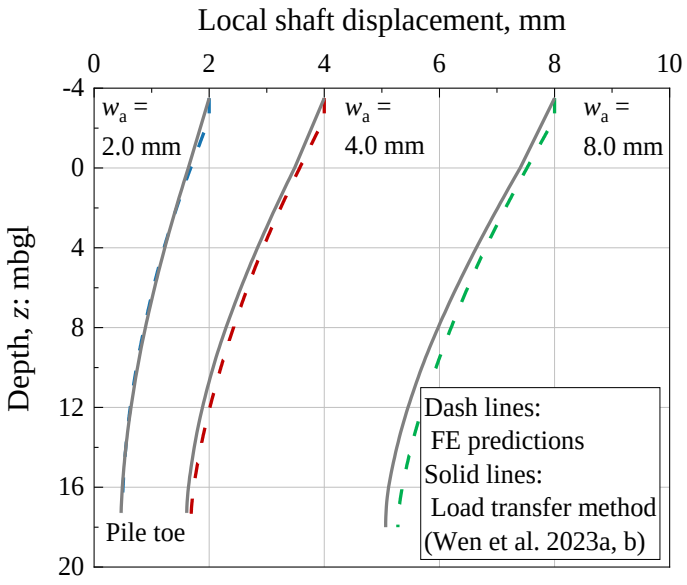
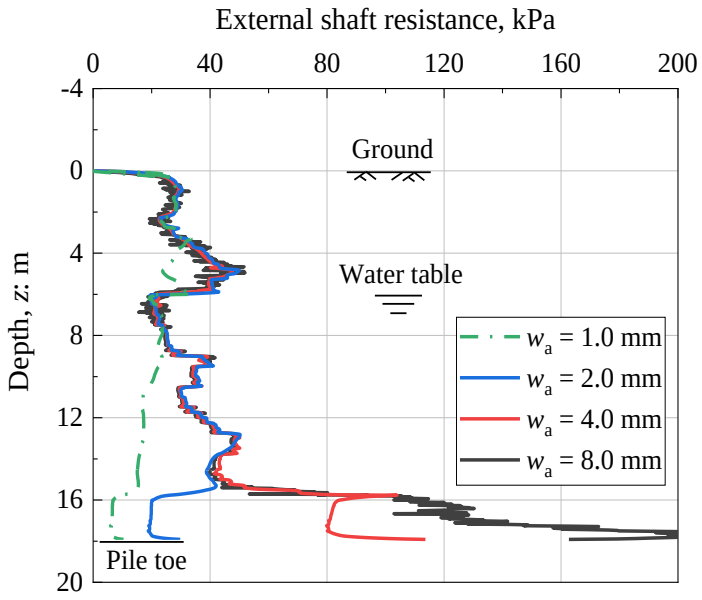


Figure 9 Profiles of local shaft displacement at various loading phases



461

462 Figure 10 Profiles of external local shaft resistances at four loading phases

463 ***Predicted mechanical response of chalk around Pile TP1***

464 This section investigates the mechanical response of the chalk domain near pile TP1 during axial
465 loading, from the perspectives of effective stress paths, stiffness degradation, variations of deviatoric
466 strain and hardening parameters' (c'). Six chalk elements located in the Zones A, B and C were selected
467 at two different depths respectively (z = 4.0 m bgl and 15.5 m bgl.), as illustrated in Figure 11. One
468 additional horizontal cross-section at a depth of 4 m bgl is selected for further investigation.

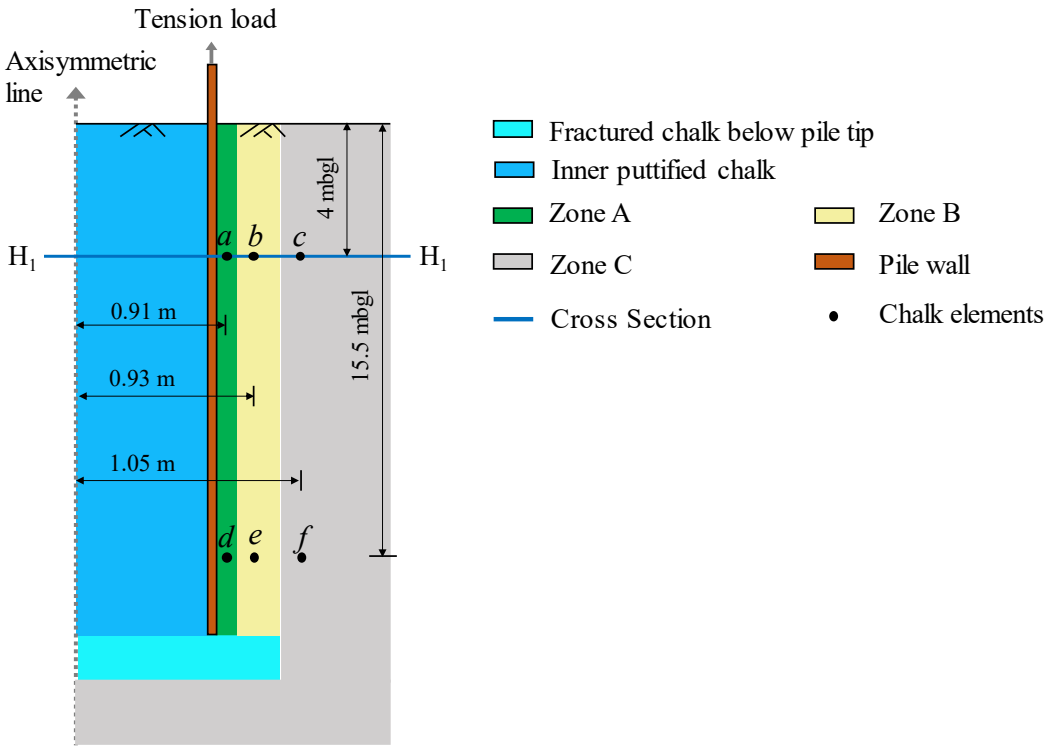


Figure 11 Positions of representative chalk elements and cross sections in chalk domain (not to scale)

Figure 12 plots the effective stress paths at six chalk elements near the pile TP1. Two elements in Zone A (puttified chalk) start from geostatic condition (K_0 stress state) in $p' - q$ stress plane, followed by sharp drops in mean effective stresses as the cavity in the pile shaft area was activated. Increments in p' is then observed due to the explicit application of external radial effective stress on the side of the cavity. Once the tension loading was imposed, it is clear that the deviatoric stress q increases, directing the stress path towards the yield/failure line. Since the strain-softening characteristics are predefined for Zones B and C, it is possible to plot their corresponding peak failure lines in the $p' - q$ plane, as shown in Figure 12(b) and 11(c). The representative stress paths plotted for both zones do not reach the predefined peak failure lines at the end of loading, implying that the chalk response in Zones B and C remains within the nonlinear elastic range (far from the strain-softening range). It appears that the pile's axial capacity is governed by the relatively weak puttified chalk in Zone A and the pile-chalk interface

failure criteria applied. Although not shown here, Wen (2023) found that the shear modulus degradation (G_{tan}/G_0) defined by Equations 4-6 did not reduce to the predetermined minimum value of 0.2 within the fractured Zone B. Stiffness degradation was not observed for Zone C intact chalk.

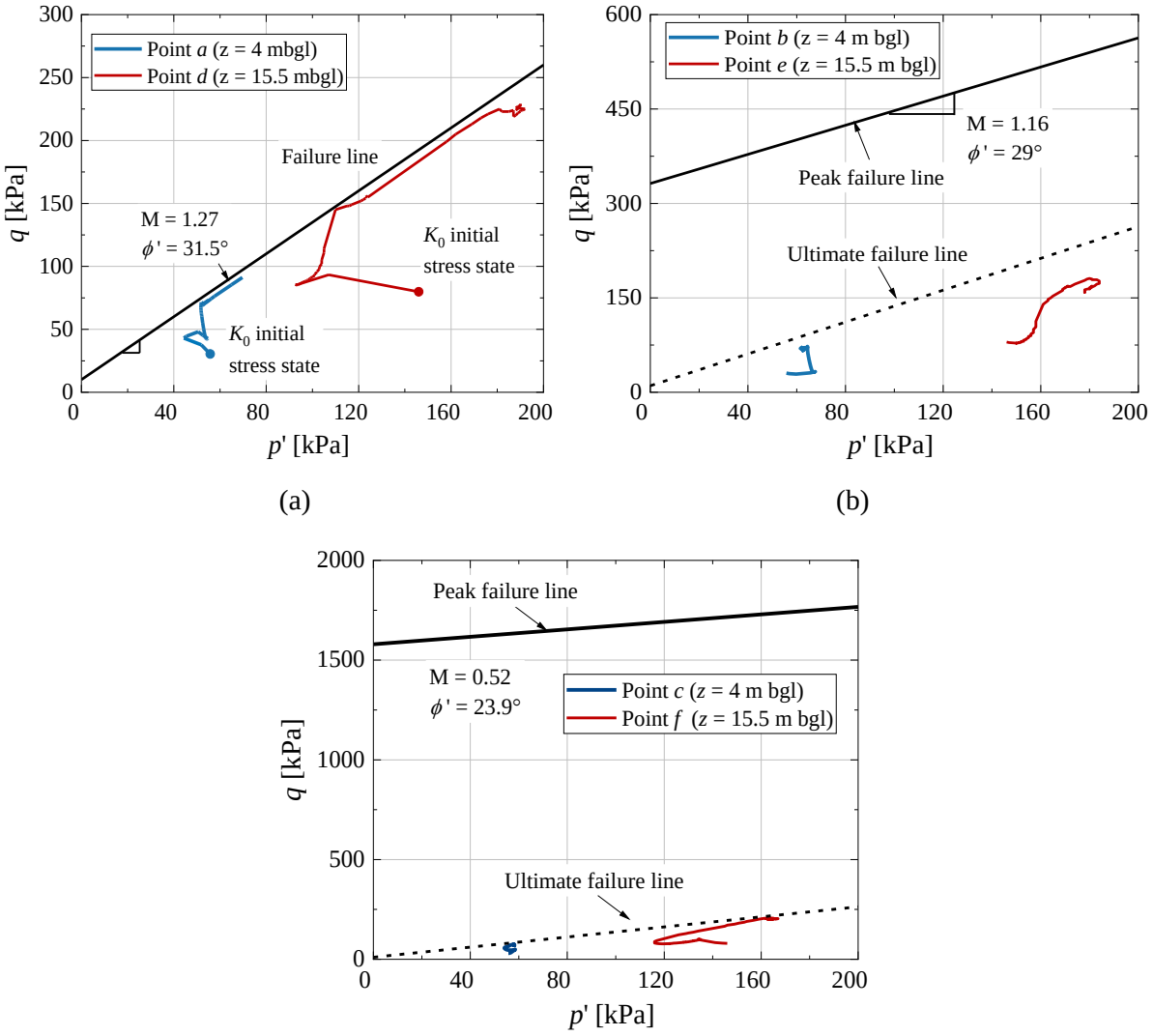


Figure 12 Stress paths of the representative chalk elements in p'-q plane: (a) Zone A; (b) Zone B; (c) Zone C

Figure 13 plots the evolution of σ'_r , σ'_v , σ'_θ at the Point *a* throughout the four predefined calculation phases that were divided into a series of calculation steps. Note that the compressive stresses are considered to be negative. Since the first calculation phase referred to the simulation of the in-situ

geostatic condition, $\sigma'_r = \sigma'_\theta$ was initially linked to the vertical component σ'_v through the predefined K_0. The σ'_r component grows from the undisturbed in-situ value to the ALAPCA-SNW pre-loading value at the end of Phase 2, while the σ'_v and σ'_θ components exhibit sharp reductions probably due to the stress-redistribution related to the excavation of intact chalk prior to the activation of the pile in Phase 2 (see Figure 2). The shear stress component τ_{rz} grows during axial tension loading from near zero to peak failure at around 37.2 kPa, followed by a minor reduction as additional displacement develop.

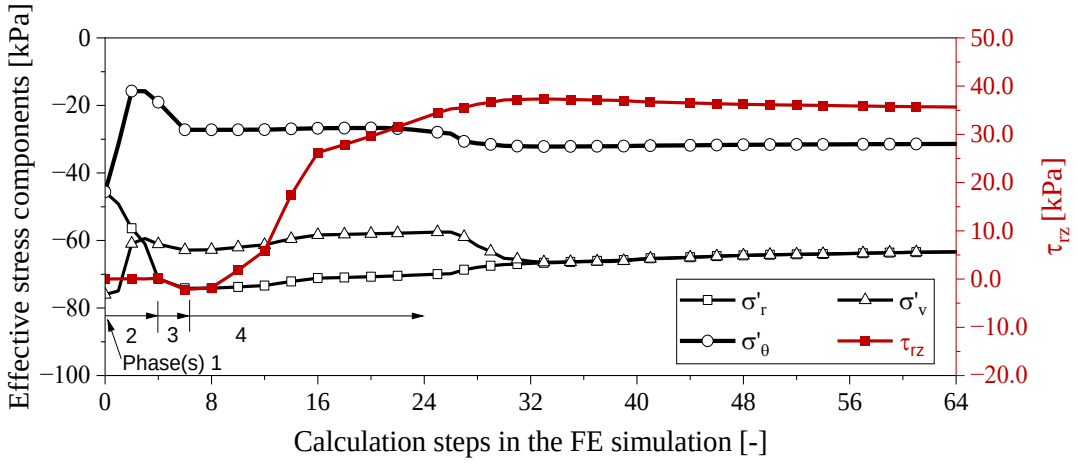
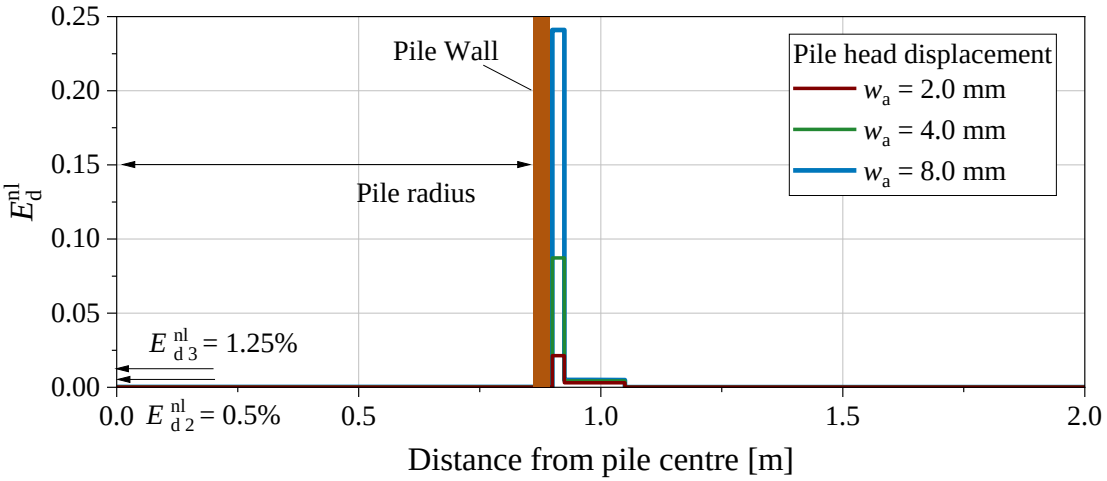


Figure 13 Evolution of σ'_r , σ'_v , σ'_θ and τ_{rz} at the Point *a* (z = 4.0 mbgl) throughout the numerical simulation with reference to the calculation phases described in Figure 2

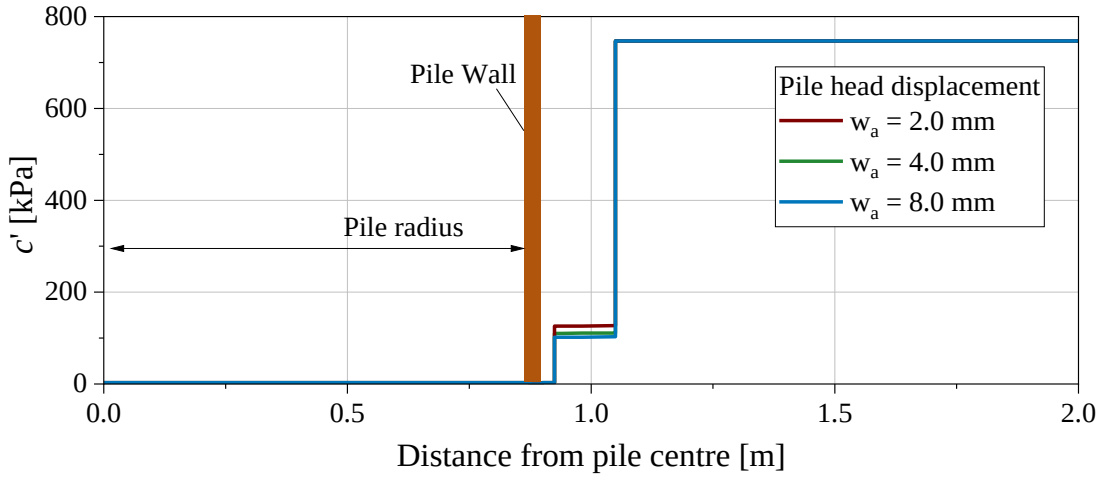
Figure 14 (a) plots the variations of the non-local deviatoric strain E_d^{nl} with radial distance from the pile centre (Cross Section $H_1 - H_1$ at 4.0 mbgl.) at three representative loading phases. Note that E_d^{nl} controls the evolution of hardening parameters in the adopted constitutive model, as discussed later. Very limited variations in E_d^{nl} were observed in the fractured and intact chalk zones, supporting the argument from the earlier stress path diagrams that the chalk's stress state in these zones falls far below the failure lines. Since the values of E_d^{nl} fell within the range of $E_{d,2}^{nl}$ =0.5% to $E_{d,3}^{nl}$ =1.25%, strain-softening (strength reduction) appeared to be only partly activated in the fractured chalk zone. Nevertheless, the strength

of the fractured chalk has not reached its residual state, given that E_d^{nl} is much lower than 1.25%. E_d^{nl} appeared to increase significantly within the thin Zone A as the loading level increased, implying that the axial response of TP1 was dominated by this Zone. It is interesting that the internal puttified chalk zone played a minor role, corresponding to the predicted lower relative displacements between the pile wall and internal puttified chalk during tension loading.

Figure 14 (b) plots the corresponding trends for c' along the specific Cross Section H_1–H_1 at three representative loading phases. As the perfectly plastic failure criterion was applied to the puttified chalk (both in Zone A and in the plug), the current c' values developed in these zones remain constant (around 3 kPa). As the E_d^{nl} profiles (see Figure 14(a)) remain far below the critical $E_{d,2}^{nl}$ value, degradation of c' was negligible in Zones B and C. Although not presented here, the evolving hardening parameter φ' also indicated negligible degradation under tension loading. The mechanical properties of the Zones B and C chalk masses impacted minorly the pile's globally non-linear response under tension loading.



(a)



(b)

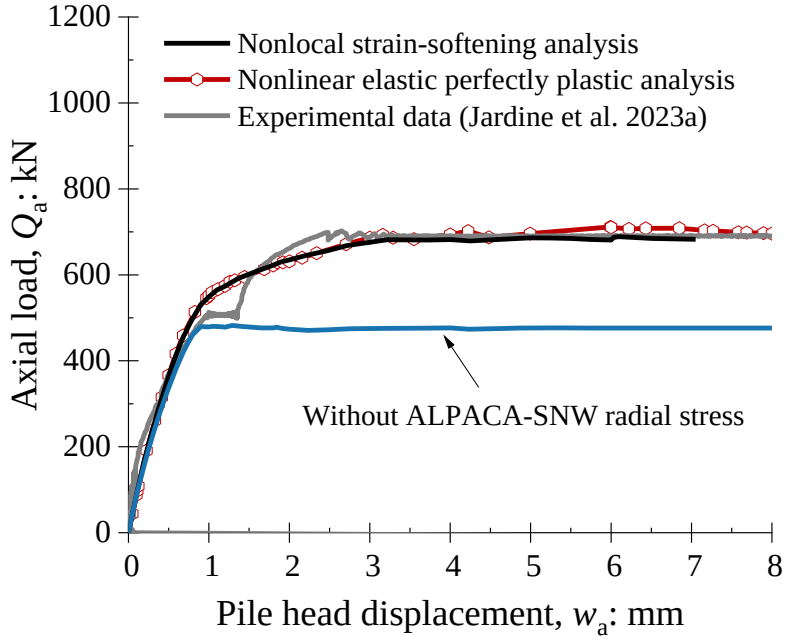
Figure 14 Mobilisation of constitutive model parameters across the $H_1 - H_1$ section with the development of pile head displacement: (a) Non-local deviatoric strain E_d^{nl}; (b) Cohesion c'

RATIO OF COMPRESSION TO TENSION PILE SHAFT CAPACITY

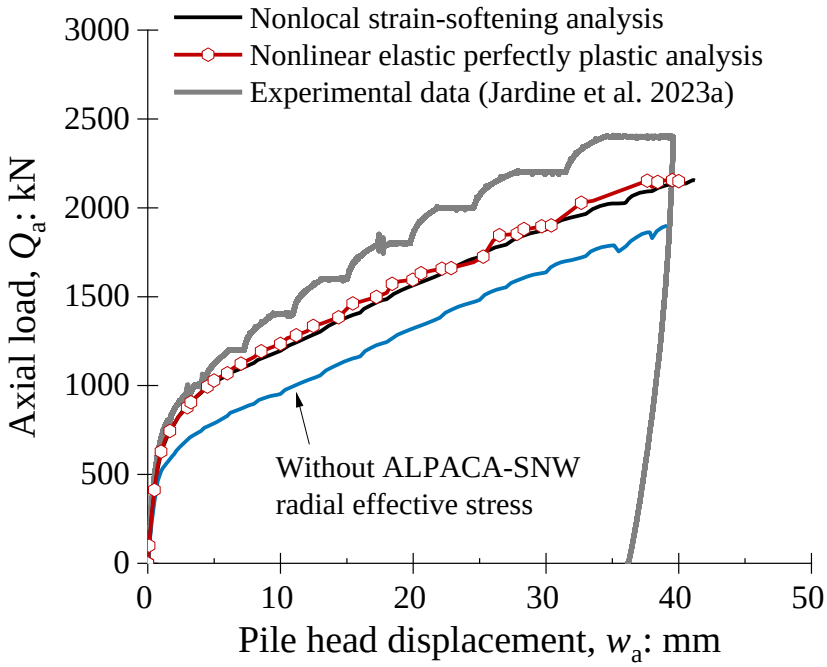
Jardine et al. (2023a, 2023b) reported that loading direction has crucial impact on driven pile's axial shaft capacity in chalk. This was explored in the present study by conducting additional FE simulations of the tension and compression tests performed on the nominally identical piles LD06 and LD07, which had smaller diameters and shorter lengths than those of TP1 pile (see Table 1). In this section, the same modelling strategy, constitutive model and chalk properties were adopted as for the TP1 pile.

Figure 15 compares the experimental and numerically predicted load-displacement response for the two piles. Reasonable agreement is observed in terms of ultimate tension capacity and stiffness evolution for the pile LD06, using the nonlocal strain-softening model. However, for the compression pile LD07, a reasonable match with the field data only take place for $w_a \leq 3.0$ mm, while the stiffness evolution is underestimated as w_a increases. As with the pile TP1, the 'nonlinear elastic perfectly plastic' analyses produce comparable axial loading response with the 'nonlocal strain-softening' analyses throughout

either compression or tension loading. It is also clear that the load-displacement responses were underestimated for piles LD06 and LD07 without applying the ALPACA-SNW radial effective stress.



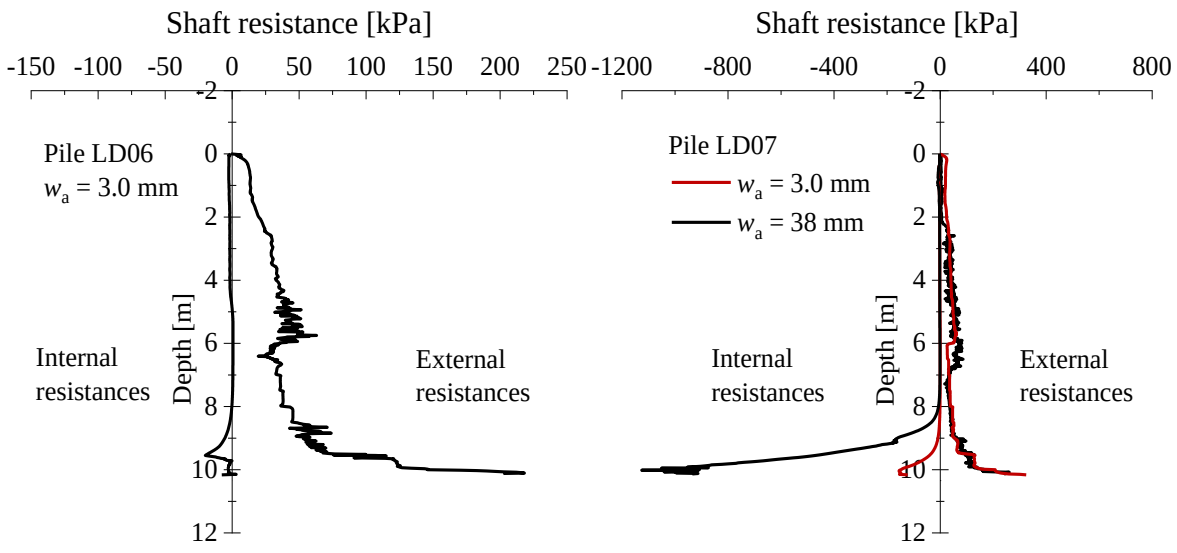
(a)



(b)

Figure 15 (a) Comparison between experimental and numerical load-displacement curves: (a) the LD06 tension pile; (b) the LD07 compression pile

549 Figure 16 shows the calculated profiles of local shaft resistances for piles LD06 and LD07 at various
550 pile head displacements, distinguishing internal and external components. Note that the negative sign
551 in Figure 16 was only used to distinguish the internal and external resistances and does not represent
552 the actual direction of the shaft resistance. At $w_a = 3$ mm, the pile LD07 simulation predicts
553 consistently higher external shaft resistances than the pile LD06, especially at shallow depths and near
554 the tip. As set out in Table 5, integrating the shaft resistances over depth gives pile external capacities
555 of around 743 kN and 646 kN in compression and tension cases respectively, which can be related to
556 Poisson's straining effects, as a result of an increase in pile radius during compression loading and a
557 reduction in pile radius under tension loading (De Nicola & Randolph, 1993). In terms of the internal
558 shaft resistances, noticeably high values concentrate towards the tip of LD07 pile, while negligible
559 values are noted at levels more than 2D above the tip. At $w_a = 3$ mm, the internal shaft capacity resisted
560 by the full chalk plug within the LD07 pile is around four times greater than for LD06 pile, leading to
561 a compression/tension shaft capacity ratio ($R_{c,t}$) of roughly 1.30. As seen in Figure 16 (b), a noticeable
562 rise in the inner shaft resistance for the pile LD07 was observed as the w_a further increases, while a
563 negligible impact on the external shaft resistance is observed. Consequently, at $w_a = 38$ mm, the
564 calculated $R_{c,t}$ value increases up to 2.64, which is mainly attributed to the considerable growth in the
565 inner shaft resistance. Note that Vinck et al. (2023b) reported a $R_{c,t}$ value of around 2.0 from a field
566 test at the 'LEMS' test site at Sauchay in Northwestern France, where the internal chalk plug had been
567 removed to a depth close to the tip.



(a) (b)

Figure 16 Profiles of calculated external/internal shaft resistances (a) the pile LD06; (b) the pile LD07

Table 5 Summary of pile inner/external shaft capacities and the corresponding compression/tension capacity ratios

Pile Code	w_a = 3.0 mm			w_a = 38.0 mm		
	Inner shaft capacity [kN]	External shaft capacity [kN]	Total shaft capacity [kN]	Inner shaft capacity [kN]	External shaft capacity [kN]	Total shaft capacity [kN]
LD06	27	646	673	27	646	673
LD07	134	743	877	1072.5	705	1778
Compression/ tension	-	1.15	1.30	-	1.09	2.64

Figure 17 compares the profiles of total (external + internal) shaft resistances from numerical models and field pile load tests at SNW. As for LD06 pile, the total shaft resistances show a broadly reasonable match with the experimental data when pile was failed. For the compression LD07 pile, the predicted shaft resistances above 9.0 mbgl are generally comparable to measured data at $w_a = 38$ mm. While direct comparison between FE and experimental data is difficult near to the pile tip where strain gauges were not deployed as a result of concerns regarding damage during pile driving, the FE simulations are broadly consistent with the field profile interpreted by Jardine et al. (2023a) on the basis of all available evidence, including tests on other piles that had strain gauges deployed closer to their tips.

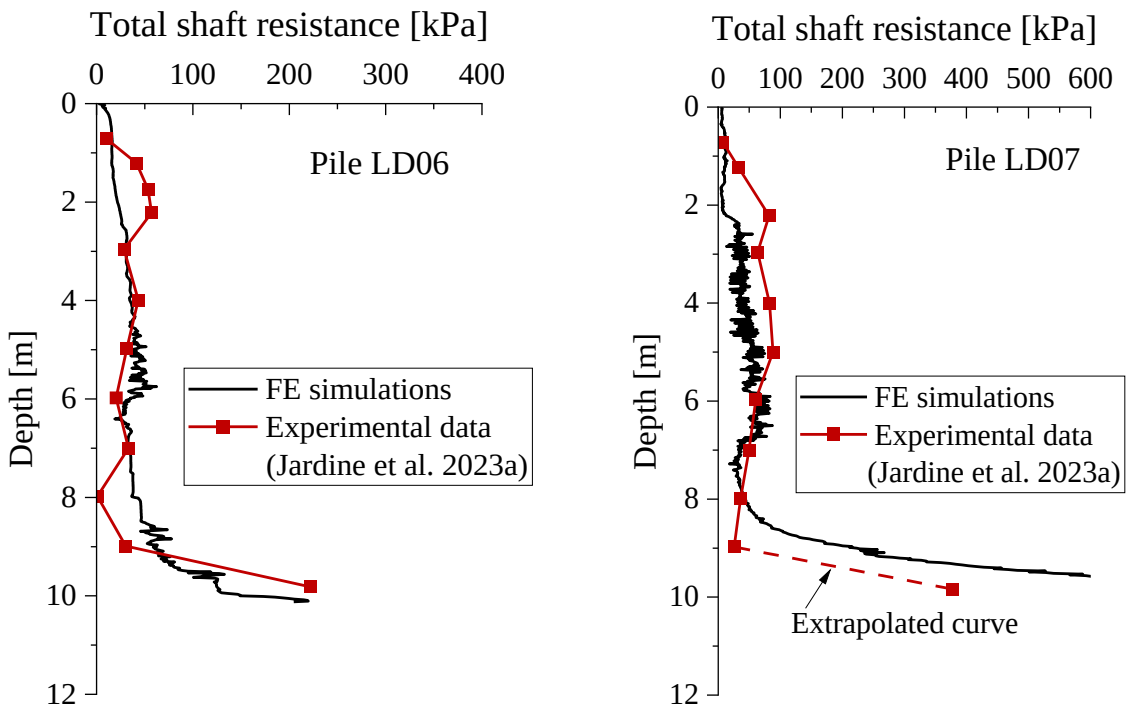
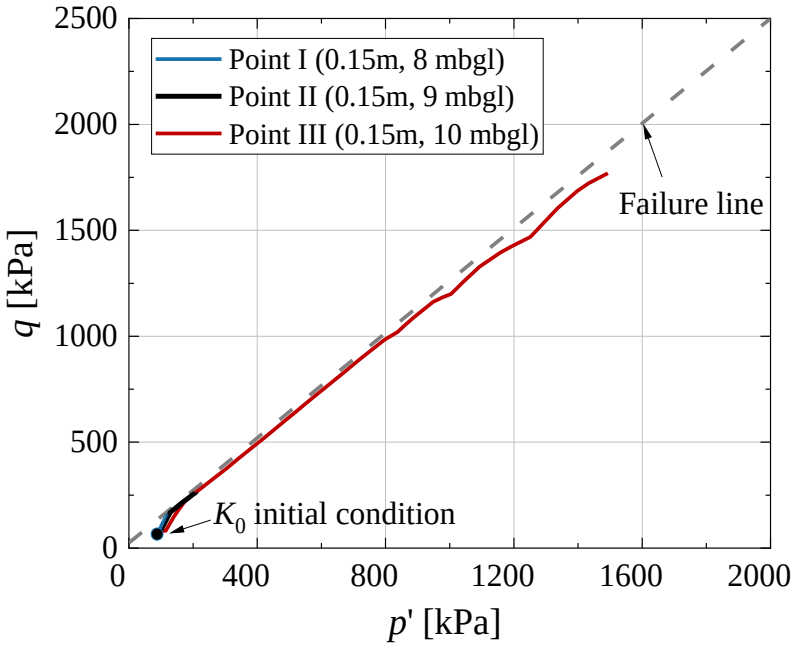


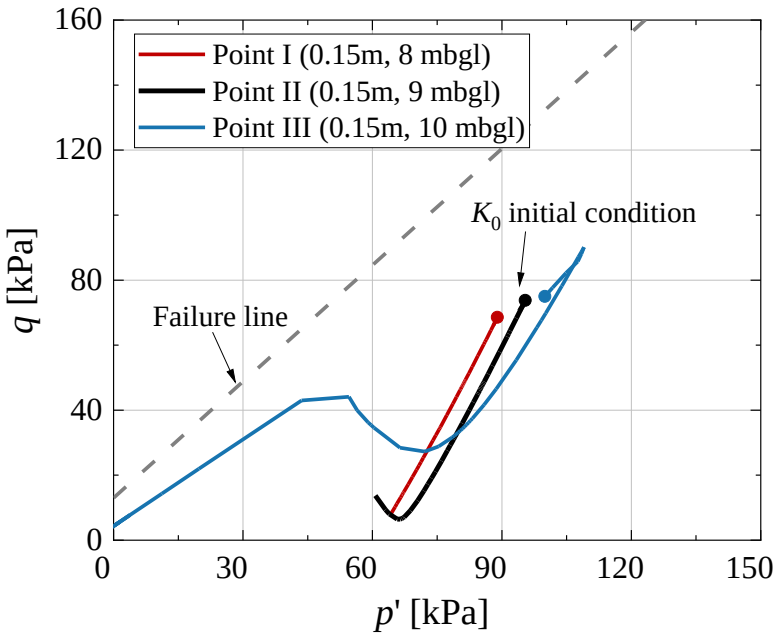
Figure 17 Comparison of total shaft resistance between numerical and experimental data; (a) the pile LD06; (b) the pile LD07

In order to comprehend the mechanism behind the marked difference in the internal shaft resistance profiles at the level of around 2D above the pile tip, three representative stress points were selected at

the locations (0.15 m from pile axis, 8 m bgl), (0.15 m, 9 m bgl) and (0.15 m, 10 m bgl), referred to as Point I, II, III respectively. Their stress paths in the $p' - q$ plane are shown in Figure 18, corresponding to compression and tension piles respectively. In the compression pile simulation, as the axial loading increases, these stress points gradually move from the initial K_0 condition towards the failure line. The Point III then experiences a marked rise in the mean effective stress (p') as compared to the remaining stress points. This is perhaps attributed to the downward movements of puttified chalk plug being constrained by the pile wall and the fractured chalk beneath pile tip (which has distinct mechanical properties from the puttified chalk plug). The higher p' levels applying near the pile tip allow growth of the deviatoric stress and high internal shaft resistances in that region. However, in the tension loading case, the same stress points generally exhibit decreasing trends of p', as shown in Figure 18(b) and the entire puttified plug eventually moves upwards together with the pile wall as tension failure occurs.



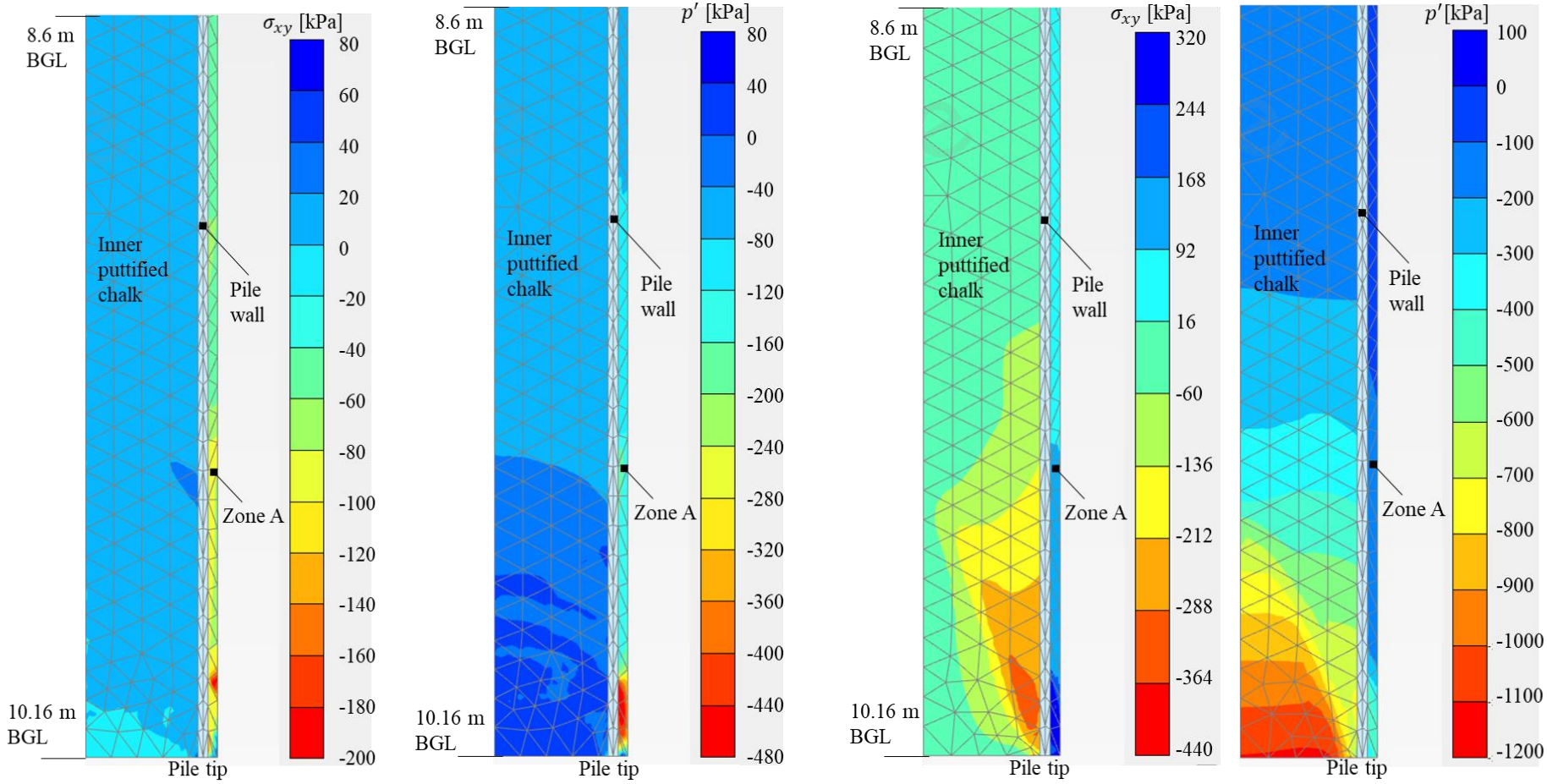
(a)



(b)

Figure 18 Stress paths of representative chalk elements in the puttified chalk plug: (a) compression case; (b) tension case

Figure 19 shows contours for three stress components (τ_{rz} and p') at the 8.6 m -10.2 m bgl levels, for both the tension and compression piles. For the sake of illustration, only the puttified chalk inside the pile, Pile wall and Zone A are presented, while other zones are hidden. In tension cases, rather lower shear stress τ_{rz} is identified along the pile-inner chalk interface, consistent with the stress paths shown in Figure 18. Unlike the tension case, markedly higher shear stresses τ_{rz} develop in the puttified chalk plug near the pile tip, which can be linked to the distribution of internal shaft resistances in Figure 17. Overall, the compression pile exhibits far higher values of p' in the puttified chalk plug than for the tension pile, probably attributed to the radial movements of the internal plug being constrained by the pile wall and the vertical movements by the fractured chalk below the pile tip.



(a) (b)

Figure 19 The τ_{rz} (σ_{xy}) and p' contour in the inner puttified chalk plug and Zone A (8.6 – 10.2 mbgl): (a) pile LD06; (b) pile LD07

SUMMARY & CONCLUSIONS

This paper presents finite element analyses of open steel pipe piles tested in the low-to-medium density chalk under axial loading under the ALPACA research programmes. Successful FE simulations rely on the appropriate division of chalk domain in the pile vicinity after installation. These comprise a thin annular zone of destructured, puttified chalk (Zone A) and a second, thicker annular zone of highly fractured chalk (Zone B), both attributed different mechanical properties compared to the surrounding parent intact chalk mass (Zone C). Following laboratory element tests, the fractured and intact chalk were modelled with a nonlinear elastic, strain-softening Mohr-Coulomb model along with nonlocal regularisation, while the puttified chalk was assumed as a non-linear elastic perfectly plastic material. The numerical results shed light in the axial load displacement behaviour of piles driven in chalk, leading to the following main points.

1. Simulation of axially loaded piles as 'wished-in-place' in geostatic chalk ground leads to significant underestimation of axial pile capacity compared to field measurements and to an unreliable pile loading displacement response. A hybrid approach proposed in this study, in which the long-term ALPACA-SNW empirical expression is used for the indirect simulation of pile installation and ageing, imposing a radial shaft stress profile to the interior of the pile shaft area in the pre-monotonic loading phases. This hybrid approach leads to good agreement with the field measurements.

2. Rigorous simulation of the pile-chalk interface plays a key role in modelling the axial pile loading response. Even when the chalk is modelled by a relatively advanced constitutive model (as in the present research) the pile-chalk interface behaviour remains governed by a simple

Coulomb failure criterion. Conducting sensitivity analysis regarding the interface strength and stiffness properties is suggested to select suitable combination of parameters to achieve satisfactory agreement to the field measurements.

3. The numerical results indicate that the puttified chalk (in Zone A) plays a dominant role in defining the axial pile shaft loading response, which is relatively insensitive to the response invoked in the fractured and intact chalk (Zone B and Zone C). The use of non-local strain-softening in the Zones B and C chalk had only a limited influence on the axial pile response.

4. Numerical simulations indicate partially why field pile shaft capacities may vary strongly with loading direction (tension or compression). It can be explained by the Poisson straining of the steel pile wall and the four times higher internal shaft resistance developed (near the tip) under compression loading than tension loading. The latter factor shows growth with compressive pile displacement and appears insensitive to the Poisson's ratio of the puttified chalk.

DECLARATION OF COMPETING INTEREST

The authors declare that they have no known competing financial interests or personal relationships that could have appeared to influence the work reported in this paper.

DATA AVAILABILITY

Data will be made available on request.

ACKNOWLEDGEMENTS

The authors are indebted to the researchers and technicians at Imperial College London who contributed to the research activities as well as their colleagues and sponsors in the ALPACA and ALPACA Plus projects. The first author acknowledges the financial support of the Skempton Scholarship of the Department of Civil & Environmental Engineering at Imperial College and the support from the China Scholarship Council (CSC). The second author acknowledges the support from the funding programme "MEDICUS" of the University of Patras, Greece.

REFERENCES

Bao, X., Wu, S., Liu, Z., Su, D., & Chen, X. (2022). Study on the nonlinear behavior of soil– pile interaction in liquefiable soil using 3D numerical method. Ocean Engineering, 258, 111807.

Bazant, Z. P., Belytschko, T. B., & Chang, T. P. (1984). Continuum theory for strain-softening. *Journal of Engineering Mechanics*, 110(12), 1666-1692

Bond, A. J., & Jardine, R. J. (1991). Effects of installing displacement piles in a high OCR clay. Geotechnique, 41(3), 341-363.

Buckley, R. M. (2018). The axial behaviour of displacement piles in chalk. PhD Thesis, Imperial College London, London, UK.

Buckley, R. M., Jardine, R. J., Kontoe, S., Parker, D., & Schroeder, F. C. (2018). Ageing and cyclic behaviour of axially loaded piles driven in chalk. *Géotechnique*, *68*(2), 146-161.

Buckley, R. M., Jardine, R. J., Kontoe, S., Barbosa, P., & Schroeder, F. C. (2020). Full-scale observations of dynamic and static axial responses of offshore piles driven in chalk and tills. *Géotechnique, 70*(8), 657-681.

Buckley, R.M., Jardine, R.J., Kontoe, S., J., Liu, T.F., Byrne, B.W., McAdam, R. A., Vinck, K. & Schranz, F. (2023). Axial cyclic loading of piles in low to medium density chalk. Accepted by *Geotechnique*.

Burland, J. B. (1990). On the compressibility and shear strength of natural clays. *Géotechnique*, 40(3), 329-378

Byrne, B. W., Houlsby, G. T., Burd, H. J., Gavin, K. G., Igoe, D. J. P., Jardine, R. J., Martin, C. M., McAdam, R. A., Potts, D. M., Taborda, D. M. ., Zdravković, L. 2020. PISA design model for monopiles for offshore wind turbines: application to a stiff glacial clay till. *Géotechnique*, 70 (11), 1030-1047.

Ciantia, M.., O'Sullivan, C., & Jardine, R. J. (2019). Pile penetration in crushable soils: Insights from micromechanical modelling. In Proceedings of the XVII ECSMGE-2019, Reykjavik, Iceland.

Clayton, C. R. I., Matthews, M.C. & Heymann, G. (2002). The Chalk. In Characterisation and Engineering Properties of Natural Soils (eds. T.S. Tan, K.K. Phoon, D.W. Hight and S. Leroueil. A.A. Balkema, Lisse). pp. 1402-1434. Singapore.

Doughty, L. J., Buckley, R. M., & Jardine, R. J. (2018). Investigating the effect of ageing on the behaviour of chalk putty. Investigating the effect of ageing on the behaviour of chalk putty. In Engineering in Chalk, London, UK. pp. 695–701.

Eringen, A. C. (1981). On nonlocal plasticity. International Journal of Engineering Science, 19(12), 1461-1474.

Galavi, V., & Schweiger, H. F. (2010). Nonlocal multilaminate model for strain softening analysis. International Journal of Geomechanics, 10(1), 30-44.

Han, F., Salgado, R., & Prezzi, M. (2018). Numerical and experimental study of axially loaded non-displacement piles in sand. In *Proc., Int. Conf. on Deep Foundations and Ground Improvement* (pp. 221-229).

Hu, Q., Han, F., Prezzi, M., Salgado, R., & Zhao, M. (2022). Finite-element analysis of the lateral load response of monopiles in layered sand. Journal of Geotechnical and Geoenvironmental Engineering, 148(4), 04022001.

Jardine, R.J. & Potts, D.M. (1988). Hutton Tension Leg Platform foundations: an approach to the prediction of driven pile behaviour. Géotechnique, 38 (2): 231- 252.

Jardine, R. J. & Potts, D. M. (1993). Magnus foundations: Soil properties and predictions of field behaviour. In Proceedings of ICE conference: large-scale pile tests in clay (ed. J. Clarke), pp. 69–83. London, UK: Thomas Telford.

Jardine, R., Chow, F., Overy, R., and Standing, J. (2005). ICP design methods for driven piles in sands and clays. London: Thomas Telford.

Jardine, R. J., Zhu, B. T., Foray, P., & Yang, Z. X. (2013). Interpretation of stress measurements made around closed-ended displacement piles in sand. Géotechnique, 63(8), 613-627

Jardine R. J., Buckley, R. M., Kontoe, S., Barbosa, P. and Schroeder, F. C. (2018). Behaviour of piles driven in chalk. Keynote, Engineering in Chalk; Eds Lawrence et al. Pub. ICE London, pp. 33-52. https://www.icevirtuallibrary.com/doi/abs/10.1680/eiccf.64072.033

Jardine, R. J., Kontoe, S., T., Liu, Vinck, K., Byrne, B. W., McAdam, R. A., Schranz, F., Andolfsson and Buckley, R. M. (2019). The ALPACA research project to improve design of piles driven in chalk. Improving the design of piles driven in chalk through the ALPACA research project. Proceedings of the 17th. European Conference on Soil Mechanics and Geotechnical Engineering, Reykjavik, Iceland. https://doi.org/10.1051/geotech/2019008

Jardine, R. J., Buckley, R. M., Liu, T., Byrne, B. W., Kontoe, S., McAdam, R. A., Schranz, F. and Vinck, K. (2023a). The axial behaviour of piles driven in chalk. Géotechnique, Ahead of print. https://doi.org/10.1680/jgeot.22.00041

Jardine, R.J., Buckley, R. M., Liu, T., Byrne, B.W., Kontoe, S., McAdam, R.A., Schranz, F. and Vinck, K. (2023b). Driven pile behaviour in low-to-medium density chalk: the ALPACA JIP outcomes. Proceedings of the 9th International Conference on Offshore Site Investigations and Geotechnics, September 2023, SUT London.

Johnson, K., Karunasena, W., Sivakugan, N., & Guazzo, A. (2001). Modeling pile-soil interaction using contact surfaces. In Computational mechanics–New frontiers for the New millennium (edited by S. Valliappan and N. Khalili), 375–380. London: Elsevier.

Liu, T., Ferreira, P. M., Vinck, K., Coop, M. R., Jardine, R. J., & Kontoe, S. (2023). The behaviour of a low-to medium-density chalk under a wide range of pressure conditions. Soils and Foundations, 63(1), 101268.

Lord J. A., Clayton, C. R. l. & Mortimore, R. N. (2002). Engineering in chalk, Report, C574. London, UK: Construction Industry Research and Information Association (CIRIA)

737 Nejjar, K., Boffa, A., Dias, D., Cuira, F., Vidil, P., Le Bissonnais, H., & Chapron, G. (2019).
738 Performance and modelling of a deep excavation in the context of the Grand Paris project. doi:
739 10.32075/17ECSMGE-2019-0415

740 Nguyen, D. D. C., Jo, S. B., & Kim, D. S. (2013). Design method of piled-raft foundations under vertical
741 load considering interaction effects. Computers and Geotechnics, 47, 16- 27.

742 Pedone, G., Kontoe, S., Zdravković, L., Jardine, R. J., Vinck, K., Liu, T. (2023a). Numerical modelling
743 of laterally loaded piles driven in low-to-medium density fractured chalk. Computers and
744 Geotechnics, 156, 105252.

745 Pedone, G., Kontoe, S., Zdravkovic, L., Jardine, R., & Potts, D. (2023b). A sensitivity study on the
746 mechanical properties of interface elements adopted in finite element analyses to simulate the
747 interaction between soil and laterally loaded piles. In *Proc. 10th European Conference on*
748 *Numerical Methods in Geotechnical Engineering* (Eds: Zdravković, L., Konte, S., Taborda,
749 D. M. G., et al.), London, UK. https://doi.org/10.53243/NUMGE2023-148

750 Plaxis, B. V. (2022). Plaxis 2D reference manual. Delft, Netherlands: Plaxis

751 Previtali, M., Ciantia, M. O. & Riccio, T. (2023). Numerical installation of OE piles in soft rocks within
752 the GPFEM framework. In Proc. 10th European Conference on Numerical Methods in
753 Geotechnical Engineering (Eds: Zdravković, L., Konte, S., Taborda, D. M. G., et al.), London,
754 UK. https://doi.org/10.53243/NUMGE2023-322

755 Said, I. D., De Gennaro, V., & Frank, R. (2009). Axisymmetric finite element analysis of pile loading
756 tests. Computers and Geotechnics, 36(1-2), 6-19.

757 Schwamb, T., & Soga, K. (2015). Numerical modelling of a deep circular excavation at Abbey Mills in
758 London. Géotechnique, 65(7), 604-619.

759 Summersgill, F. C., Kontoe, S., & Potts, D. M. (2017a). Critical assessment of nonlocal strain-softening
760 methods in biaxial compression. International Journal of Geomechanics, 17(7), 04017006.

761 Summersgill, F. C., Kontoe, S., & Potts, D. M. (2017b). On the use of nonlocal regularisation in slope
762 stability problems. Computers and Geotechnics, 82, 187-200.

763 Taborda, D. M., Potts, D. M., Zdravković, L. (2016). n the assessment of energy dissipated through
764 hysteresis in finite element analysis. Computers and Geotechnics, 71, 180-194.

765 Taborda, D. M., Zdravković, L., Potts, D. M., Burd, H. J., Byrne, B. W., Gavin, K. G., ... & McAdam,
766 R. A. (2020). Finite-element modelling of laterally loaded piles in a dense marine sand at
767 Dunkirk. Géotechnique, 70(11), 1014-1029.

768 Taborda, DMG, Kontoe, S, Tsiampousi, A (2022a). IC MAGE Model 01 –strain hardening/softening
769 Mohr-Coulomb failure criterion with isotropic small strain stiffness (Version 1.7). Zenodo.
770 doi:10.5281/zenodo.7198927

771 Taborda, DMG, Kontoe, S, Tsiampousi, A (2022b). IC MAGE UMIP –universal model interface for
772 PLAXIS (Version 3.2). Zenodo. doi: 10.5281/zenodo.7129726

Vermeer, P. A., & Brinkgreve, R. B. J. (1994). A new effective nonlocal strain measure form softening plasticity. In International workshop on localisation and bifuration theory for soils and rocks. (Eds. Chambon, R., Desrues, J., Vardoulakis, I.), pp: 89-100. Balkema, Rotterdam, Netherlands.

Vinck, K. (2021). Advanced geotechnical characterisation to support driven pile design at chalk sites. PhD Thesis, Imperial College London, London, UK.

Vinck, K., Liu, T., Jardine, R. J., Kontoe, S., Ahmadi-Naghadeh, R., Buckley, R. M., Byrne, B. W., Lawrence, J., Mcadam, R. A. & Schranz, F. (2022). Advanced in-situ and laboratory characterisation of the ALPACA chalk research site. Géotechnique, 1-15. https://doi.org/10.1680/jgeot.21.00197

Vinck, K., Liu, T., Jardine, R. J., Byrne, B. W. & Willow A. (2023a). The effects of steel corrosion on the interface shearing behaviour of chalk. Proceedings of 9th Int. Conf on Offshore site Investigations and Geotechnics. Pages 1282-1289. Society for Underwater Technology (SUT), London.

Vinck, K., Liu, T., Mawet, J., Kontoe, S. and Jardine R. J. (2023b). Field tests on large scale instrumented piles driven in chalk: results and interpretation. *Canadian Geotechnical Journal*, https://doi.org/10.1139/cgj-2022-0441

Wang, J., & Zhao, B. (2014). Discrete-continuum analysis of monotonic pile penetration in crushable sands. Canadian Geotechnical Journal, 51(10), 1095-1110.

Wen, K. (2023). Dynamic and monotonic axial loading responses of piles driven for offshore wind turbines. PhD Thesis, Department of civil and Environmental Engineering, Imperial College London, London, UK.

Wen, K., Kontoe, S., Jardine R. J., Liu, T. (2023a). An axial load transfer model for piles driven in chalk. *Journal of Geotechnical and Geoenvironmental Engineering*. https://doi.org/10.1061/JGGEFK.GTENG-11368

Wen K., Kontoe, S., Jardine, R. J. & Liu, T. (2023b). A new load transfer model for axially loaded piles driven in chalk. *Proc. 9th Int. Conf. on Offshore Site Investigations and Geotechnics*. London, UK: Society for Underwater Technology (SUT).

Wen, K., Kontoe, S., Jardine, R.J., Liu, T. & Pan. L (2023c). Non-linear finite-element analysis of axially loaded piles driven in chalk. In *Proc. 10th European Conference on Numerical Methods in Geotechnical Engineering* (Eds: Zdravković, L., Konte, S., Taborda, D. M. G., et al.), London, UK. https://doi.org/10.53243/NUMGE2023-337

Yang, Z. X., Gao, Y. Y., Jardine, R. J., Guo, W. B., & Wang, D. (2020). Large deformation finite-element simulation of displacement-pile installation experiments in sand. Journal of Geotechnical and Geoenvironmental Engineering, 146(6), 04020044.

Zdravković, L., Taborda, D. M., Potts, D. M., Abadias, D., Burd, H. J., Byrne, B. W., ... Ushev, E. (2020). Finite-element modelling of laterally loaded piles in a stiff glacial clay till at Cowden. Géotechnique, 70(11), 999-1013.

Zhang, C., Yang, Z. X., Nguyen, G. D., Jardine, R. J., & Einav, I. (2014). Theoretical breakage mechanics and experimental assessment of stresses surrounding piles penetrating into dense silica sand. Géotechnique letters, 4(1), 11-16

Ziogos, A., Brown, M., Ivanovic, A., & Morgan, N. (2017). Chalk–steel interface testing for marine energy foundations. Proceedings of the Institution of Civil Engineers Geotechnical Engineering, 170(3), 285-298.

LIST OF NOTATIONS

c_i'	Interface cohesion
D	Pile outer diameter
E_d^*	Deviatoric deformation level
E_d^{nl}	Non-local deviatoric strain invariant
f_L	Loading factor
f_{tip}	Pile tip condition factor
G_0	Maximum shear modulus
h	Distance from pile tip
K_0	Earth pressure coefficient
K_s	Interface shear stiffness
K_n	Interface normal stiffness
n	Scaling factor
p'	Mean effective stress
q	Deviatoric stress
q_t	Corrected CPT tip resistance
Q_a	Axial load at pile head
$R_{c,t}$	Compression/tension shaft capacity ratio
R	Pile radius
R_G	Reduction factor determined by the deviatoric deformation level
t_w	Pile wall thickness
w_a	Pile head displacement
z	Depth from ground surface
α	Factor of the nonlocal contribution to the nonlocal strain calculation
δ'	Chalk-steel interface friction angle
σ_{rc}'	Local effective stress along the pile shaft after equalisation period
$\Delta\sigma_{rd}'$	Change in radial effective stress due to interface dilation
σ_x', σ_y', σ_z'	Effective stress in the x, y, z direction (Cartesian coordinate system)
σ'_θ	Circumferential effective stress
σ'_v	Vertical effective stress
σ_{v0}'	Vertical effective stress at geostatic state
τ_{rz}	Shear stress component
τ_{rzf}	Long-term axial shaft resistances at failure
φ_i'	Interface frictional angle
ψ_i'	Dilation angle at interface
ALPACA	Axial-Lateral Pile Analysis for Chalk Applying multi-scale field and laboratory testing
ALPHA	Numerical analysis of laterally loaded piles driven in chalk
bgl	Below ground level
DL	Defined length
JIP	Joint Industry Programmes
FBG	Fibre Bragg Grating

LIST OF TABLES

Table 1 Summary for driven piles to be simulated in this study

Table 2 Calibration of pre-yield stiffness and strength parameters applied in different chalk domains

Table 3 Strength-related parameters applied in various zones in the nonlinear elastic perfectly plastic analysis

Table 4 Parameters related to the non-local formulation and the strain-softening rate for different chalk zones

Table 5 Summary of pile inner/external shaft capacities and the corresponding compression/tension capacity ratios

LIST OF FIGURES

Figure 1 Axisymmetric FE model of TP1 pile under axial loads and the finite element mesh

Figure 2 The four calculation phases adopted for simulating driven piles in chalk

Figure 3 Variation of strength parameters c', $\varphi'$and ψ' with the current nonlocal strain (Taborda et al. 2022a, 2022b)

Figure 4 Stiffness degradation data (from Vinck 2021) and stiffness degradation curve adopted in FE analyses for 30-days aged puttified chalk (adapted from Pedone et al. 2023a)

Figure 5 Drained triaxial test on intact chalk from Vinck et al. (2022) and the derived failure envelopes (adapted from Pedone et al. 2023a)

Figure 6 Calibration of $E_{d,2}^{nl}$ and $E_{d,3}^{nl}$ parameters for: (a) fractured chalk; (b) intact chalk

Figure 7 Comparison between two cases for pile TP1: (a) radial effective stress profile; (b) variation of radial effective stress against normalised radius obtained from FE simulations

Figure 8(a) Comparison between experimental and numerical load-displacement curves; (b) comparison of axial force profiles

Figure 9 Profiles of local shaft displacement at various loading phases

Figure 10 Profile of external local shaft resistances at four loading phases

Figure 11 Positions of representative chalk elements and cross sections in chalk domain (not to scale)

Figure 12 Stress paths of the representative chalk elements in p'-q plane: (a) Zone A; (b) Zone B; (c) Zone C

Figure 13 Evolution of σ'_r , σ'_v , σ'_θ and τ_{rz} at the Point a (z = 4.0 mbgl) throughout the numerical simulation with reference to the calculation phases described in Figure 2

Figure 14 Mobilisation of constitutive model parameters across the H_1 – H_1 section with the development of pile head displacement: (a) Non-local deviatoric strain E_d^{nl}; (b) Cohesion c'

Figure 15 Comparison between experimental and numerical load-displacement curves: (a) the LD06 tension pile; (b) the LD07 compression pile

Figure 16 Profiles of calculated external/internal shaft resistances (a) the pile LD06; (b) the pile LD07

Figure 17 Comparison of total shaft resistance between numerical and experimental data; (a) the pile LD06; (b) the pile LD07

Figure 18 Stress paths of representative chalk elements in the puttified chalk plug: (a) compression case; (b) tension case

Figure 19 The τ_{rz} (σ_{xy}) and p' contour in the inner puttified chalk plug and Zone A (8.6 – 10.2 mbgl): (a) pile LD06; (b) pile LD07